J. Fluid Mech. (2025), *vol.* 1010, A21, doi:10.1017/jfm.2025.273

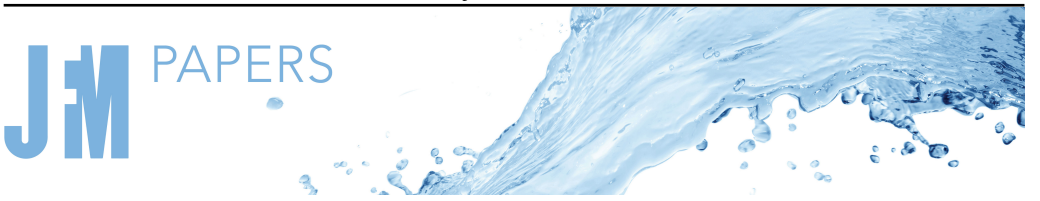

Spatial and temporal characteristics of scalar dissipation rate in a stopping turbulent jet

Vlad Aparece-Scutariu[1], **Minjun Choi**[2] and **Dong-hyuk Shin**[2]

[1]Romanian Research and Development Institute for Gas Turbines COMOTI, 220D Iuliu Maniu Ave., Bucharest 061126, Romania

[2]Department of Aerospace Engineering, Korea Advanced Institute of Science and Technology, 291 Daehak-ro, Yuseong-gu Daejon, 34141, Republic of Korea

Corresponding author: Dong-hyuk Shin, donghyuk.shin@kaist.ac.kr

(Received 12 May 2024; revised 22 January 2025; accepted 4 March 2025)

Scalar dissipation rate (SDR) evolution in a stopping turbulent jet was analysed using direct numerical simulations and a theoretical approach. After the jet is stopped, a deceleration wave for the SDR propagates downstream with a speed similar to that for axial velocity. Upstream of the deceleration wave, mean centreline SDR becomes proportional to axial distance, and inversely proportional to the square of time. After passing of the deceleration wave, normalised radial profiles of SDR and its axial, radial and azimuthal components reach self-similar states, denoted decelerating self-similar profiles, which are different from their steady-state counterparts. Production and destruction terms in the mean SDR transport equation remain dominant in the decelerating self-similar state. The theoretical approach provides an explicit prediction for the radial profile of a turbulent fluctuation term of the mean SDR transport equation. Three turbulent SDR models are validated, and modifications suitable for the decelerating jet are proposed, based on a self-similarity analysis.

Key words: turbulence modelling, jets, turbulent mixing

1. Introduction

In combustion applications, transient fuel jet injection controls ignition event timing. Flame ignition and subsequent stabilisation do not occur unless the right amounts of fuel and oxidiser are available at a given location. For example, in compression ignition engines, the ignition event occurs during the decelerating phase of fuel injection, as seen

Figure 1. Single cylinder optical engine transient fuel injection consisting, from left to right in chronological order, of a starting jet, a steady-state jet and a stopping jet, during which the ignition event happens (Gill *et al.* 2005).

in figure 1. Controlling ignition timing is essential, considering that the time-dependent behaviour of the jet flow can lead to increased/decreased air entrainment (Hill & Greene 1977; Bremhorst & Hollis 1990). An improved mixing of fuel and oxidiser is sought, as this leads to enhanced heat conversion and reduced pollutant emissions (O'Connor & Musculus 2013). However, insufficient mixing causes incomplete combustion. It follows that optimising the injection process requires a solid understanding of unsteady mixing dynamics. This motivates the present investigation to tackle, using direct numerical simulations (DNS), the less investigated topic of turbulent mixing in unsteady jets, particularly decelerating ones.

In compression ignition engines, the combustion mode takes the form of a turbulent non-premixed flame. This configuration is often modelled by two variables: mixture fraction (denoted as ξ) and scalar dissipation rate (SDR, denoted as χ). Mixture fraction is defined as the mass fraction that originates from one stream in a two-stream set-up. Typically, the two streams are fuel and oxidiser, such that ξ is considered unity at the inlet of the fuel stream, and zero at the oxidiser stream inlet. As fuel and oxidiser mix inside the combustion chamber, there will be a mixture fraction distribution. The flame can exist where the mixture fraction equals the stoichiometric mixture fraction value.

The second variable, SDR, indicates the mixedness of the flow field and is defined as

$$\chi = 2\mathfrak{D}(\boldsymbol{\nabla}\xi \cdot \boldsymbol{\nabla}\xi). \tag{1.1}$$

For industry-based applications, where Reynolds-averaged Navier–Stokes (RANS) simulations are the norm, the mean SDR is of particular interest. The SDR arises naturally from the scalar variance ($\overline{\xi'^2}$) transport equation:

$$\overline{\rho}\frac{\partial \overline{\xi'^2}}{\partial t} + \overline{\rho}\,\overline{u_j}\frac{\partial \overline{\xi'^2}}{\partial x_j} = -\frac{\partial \overline{\rho}\,\overline{u_j'\xi'^2}}{\partial x_j} + \frac{\partial}{\partial x_j}\left(\overline{\rho}\mathfrak{D}\frac{\partial \overline{\xi'^2}}{\partial x_j}\right) - 2\overline{\rho}\,\overline{u_j'\xi'}\frac{\partial \overline{\xi}}{\partial x_j} - 2\mathfrak{D}\overline{\rho}\,\overline{\frac{\partial \xi'}{\partial x_j}\frac{\partial \xi'}{\partial x_j}}. \tag{1.2}$$

For an incompressible, passive scalar flow in the high Reynolds number limit, the mean SDR is approximated as the mean dissipation rate of scalar turbulent fluctuations, $\overline{\chi} \approx 2\mathfrak{D}(\overline{\boldsymbol{\nabla}\xi' \cdot \boldsymbol{\nabla}\xi'})$ (Poinsot & Veynante 2005). As a consequence, $\overline{\chi}$ is an omnipresent and essential quantity in describing the turbulent scalar field.

In the context of compression ignition engines, the SDR is directly correlated with local flame ignition/extinction as well as with reaction rates (Mastorakos *et al.* 1997). During the injection process, turbulence acts to stretch and fold the diffusive scalar interface between the two fluid streams. This increases scalar gradients. Repeated stretching and folding increases gradients exponentially, until the scalar characteristic length scale is reduced to

a viscous limit such as the Kolmogorov or Batchelor scales (Batchelor 1953; Kolmogorov 1962). At the viscous limit, smoothing of scalar fluctuations by molecular mixing occurs. The destruction rate of scalar variance is quantified by the SDR. Figure 1 shows a sequence of fuel injections inside an engine chamber. There, ignition occurs during the decelerating phase of fuel injection, when SDR values are lower.

A widely used model for SDR in flows involving turbulent mixing is based on the similarity between the velocity and scalar fields (LaRue & Libby 1981; Ma & Warhaft 1986; Danaila *et al.* 2012), relating the SDR to an algebraic relation (Bray *et al.* 1994). This similarity exists in the context of the widely accepted Kolmogrov–Obukhov–Corrsin (KOC) theory of scalar turbulent mixing. The KOC theory hypothesises the isotropy and independence of small scales from the large scales of the scalar field. However, the KOC phenomenology has been questioned, as small scales showed departure from isotropy when the large scales were anisotropic (Warhaft 2000). Scalar field local isotropy and its violations have been reported in the literature quite often (Sreenivasan 1991). Still, a significant amount of these investigations considered scalar injection into an isotropic and homogeneous flow field, which allows us to draw a similarity between velocity and scalar fields (LaRue & Libby 1981; Ma & Warhaft 1986; Danaila *et al.* 2012).

In real configurations, turbulent flows are inhomogeneous and can exhibit time dependency or chemical reactions. This leads to discrepancies between characteristic scales of velocity and scalar fields. In such situations, algebraic-type models would require a more complex formulation (see e.g. (12) of Swaminathan & Bray 2005) or would need to be replaced with an exact transport equation for the SDR (Lumley & Khajeh-Nouri 1975; Swaminathan & Bray 2005). Individual terms of this equation consist in the time variation of $\overline{\chi}$, advective transport, the diffusive flux of $\overline{\chi}$, turbulent diffusion, the scalar field local curvature effects and local stretch, respectively.

For spatio-temporal characterisation of the SDR in the turbulent jet, the concept of self-similarity is pivotal (Pope 2000). When self-similarity holds, all normalised flow quantities can be described by a reduced number of variables. In a steady-state jet, for example, velocity statistics, scaled by the centreline axial velocity, become a function of the scaled radius, defined as the radius divided by an axial location. Experimental measurements of Hussein *et al.* (1994) show that after a given transition region, close to the jet inlet, velocity radial profiles become self-similar. The same applies for passive scalar profiles up to fourth-order moments, reported by Mi *et al.* (2001).

Although self-similarity and mixing characteristics in the steady-state jet have been widely studied (Feikema *et al.* 1996; Buch & Dahm 1998; Su & Clemens 1999; Mi *et al.* 2001; Karpetis & Barlow 2002; Fuest *et al.* 2018; Aparece-Scutariu & Shin 2022), the stopping jet has received less attention, despite its importance. Borée *et al.* (1996) reduced the velocity by half and identified a spatio-temporal similarity behaviour with a time shift. Musculus (2009) theoretically derived the entrainment wave after which the entrainment increases by three times. Shin *et al.* (2023) investigated the evolution of the mixture fraction during the decelerating stage, using the same DNS database as for the present study. Both the numerical simulation (see figure 2*a*) and a theoretical analysis showed that the mean mixture fraction ($\overline{\xi}_c$) scales with axial distance (x) and time (t) as

$$\overline{\xi}_c = C_\xi \frac{x - x_0}{t - t_0}, \tag{1.3}$$

where C_ξ is a flow-dependent constant, while x_0 and t_0 represent spatial and temporal virtual origins, respectively. Furthermore, second-order statistics ($\overline{v'\xi'}$) also remain self-similar, as shown in figure 2(*b*), whose radial profile was predicted by a theoretical derivation, assuming self-similarity (see (18) in Shin *et al.* 2023). The assumption of

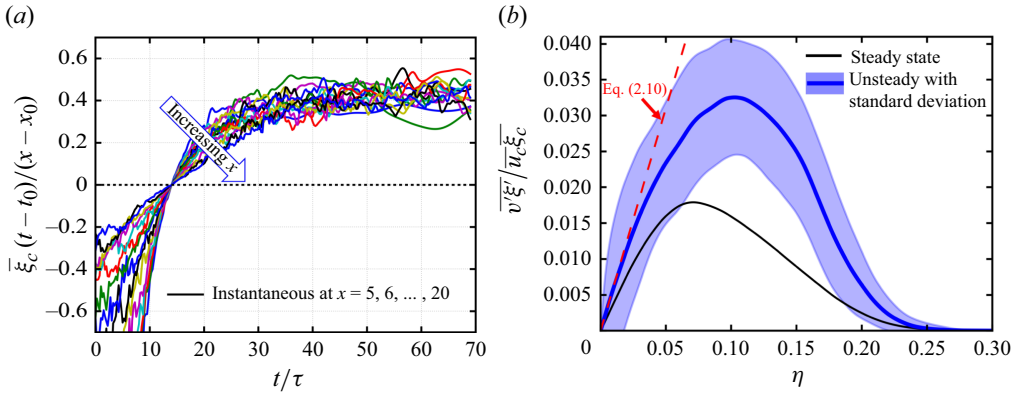

Figure 2. (*a*) Scaled centreline mixture fraction over time, at downstream locations over $x/D = 7-20$ (Shin *et al.* 2017). (*b*) Self-similar radial profiles for a stopping jet $\overline{v'\xi'}$ obtained over $12.5 < x < 20$ and $50 < t < 69$ (Shin *et al.* 2023), along with centreline slope prediction (see equation (2.10) of Shin *et al.* 2023).

self-similarity allows us to obtain radial profiles, while an integral method does not (Musculus 2009).

This paper aims to characterise the spatial and temporal evolution of the SDR of a stopping jet. First, a theoretical development is made under the assumption of self-similarity. Second, using the DNS dataset, a series of rigorous investigations is conducted to verify self-similarity of the SDR and its directional components. Third, a validation study is conducted to see if the theoretical analysis can predict a transport term. Finally, existing turbulence algebraic models are compared with the DNS dataset, and modifications are proposed.

1.1. *Literature review on SDR characteristics and modelling*

Experimental SDR measurements in turbulent flows have been the subject of significant efforts. Advancements in optical instrumentation have recently facilitated more accurate three-dimensional measurements. Karpetis & Barlow (2002) looked at SDR evolution in the case of piloted methane–air jet flames. Geyer *et al.* (2005) performed measurements of SDR in reacting and non-reacting turbulent opposing jets. Kaiser & Frank (2007) obtained two-dimensional images of near-field dissipation structures in hydrogen–methane non-premixed flames. Soulopoulos *et al.* (2014, 2015) conducted spatial SDR measurements in non-reactive starting turbulent round jets (figure 3). McManus & Sutton (2023) investigated the SDR field in non-premixed turbulent jet flames, focusing on the use of a set of conditional statistics to characterise small-scale structures, including the correlation between dissipation layer widths and temperature, the Reynolds number or dissipation magnitude. Mulla & Hardalupas (2022) carried out instantaneous three-dimensional SDR measurements in a turbulent swirling flow, validating the azimuthal component through the assumption of isotropy with the axial component.

Recent progress in computational power has allowed for an examination of turbulent mixing and SDR from a numerical perspective at Reynolds numbers significantly closer to real-world applications than in the past. Still, resolution requirements remain essential, as pointed out by Schumacher *et al.* (2005) in a DNS investigation of fine scalar mixing. The two main advantages when investigating the SDR numerically are the ability to compute the SDR in every region of the turbulent flow, and the possibility to compute all of the three directional gradients of mixture fraction without any underlying assumptions. Hawkes *et al.* (2009) used planar jet flames DNS data to obtain relationships between measured

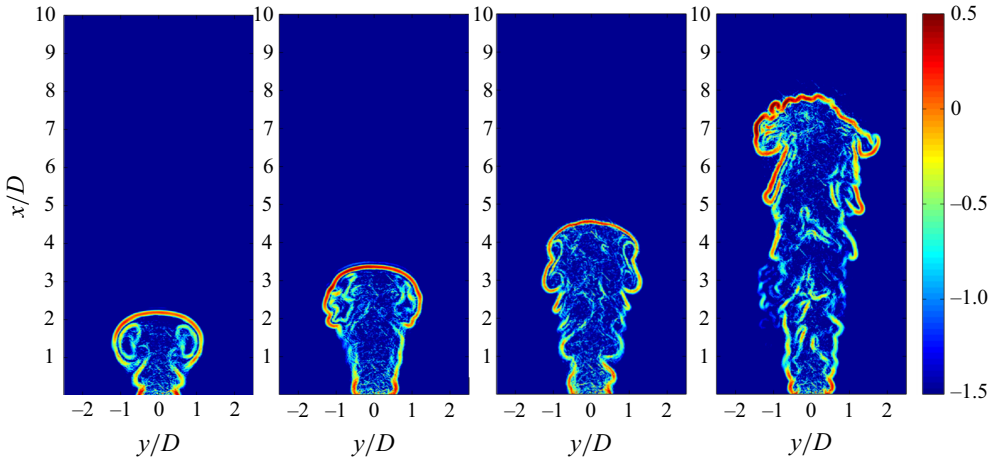

Figure 3. Snapshots of instantaneous SDR at different times after the point of starting. The snapshots are taken at non-dimensional times $t/T = 3.4, 5, 7.15, 9.65$ from top to bottom and left to right.

three-dimensional SDR values and lower-dimension estimations. These relationships were beneficial for subsequent experimental efforts targeting the SDR in jet flames (Fuest *et al.* 2018; Mulla & Hardalupas 2022), where measurement of the azimuthal component remained a complex task.

Such SDR modelling has been of continuous interest in the area of turbulent combustion, as it plays an essential role in modelling chemical reaction rates. A robust SDR model should accurately capture turbulent mixing, molecular diffusion and chemical reactions, as well as their interaction. Swaminathan & Bray (2005) proposed a model for the SDR that includes a chemical time scale besides the scalar–turbulence time scales of the model in (1.1). This was done by analysing the dominant terms of the SDR exact transport equation. The model was validated with DNS data of a premixed flame. Kolla *et al.* (2009) improved the model of Swaminathan & Bray (2005) by including the effect of dilatation rate and its influence on scalar–turbulence interaction, chemistry and molecular diffusion. The new model showed good agreement with DNS data over a range of flame conditions. Langella *et al.* (2015) used the extended algebraic model of Dunstan *et al.* (2013), which is based on the work of Kolla *et al.* (2009), for closure of filtered reaction rate in large eddy simulations (LES) of turbulent piloted methane–air Bunsen flames. The same model of Dunstan *et al.* (2013) was used by Langella & Swaminathan (2016) in unstrained and strained closures for the filtered reaction rate in LES of premixed flames. Comparison with experimental data showed good agreement for the unstrained flamelet closure and an underestimation of the burn rate in the case of the strained flamelet closure.

A transport equation for the SDR was initially derived by Lumley & Khajeh-Nouri (1975) by presuming a close to unity Prandtl number in the context of isotropic turbulence. Lumley (1976) analysed the equation for a passive scalar in buoyancy driven mixed layers. Later, its applicability was extended to chemically reacting turbulent flows (Borghi 1990; Mantel & Borghi 1994; Mura & Borghi 2003) with constant-density approximations, and also to inhomogeneous turbulence (Jones & Musonge 1988). Thermal expansion effects due to combustion were included by Swaminathan & Bray (2005) in the context of premixed flames. Derivation of a $\overline{\chi}$ equation is described by Swaminathan & Bray (2005), with Chakraborty *et al.* (2011) providing a comprehensive analysis of the SDR budget terms. The same derivation procedure of Swaminathan & Bray (2005) can be applied for a passive scalar in a constant-density turbulent jet, leading to (3.1).

The mean SDR equation has been of particular interest to the combustion community. Providing reliable models for $\overline{\chi}$ in the context of RANS simulations has been the focus of considerable research effort. Tennekes & Lumley (1972) proposed an order-of-magnitude analysis that indicates that only two of the budget are dominant and scale with the turbulent Reynolds number (3.24). The first relates to scalar–turbulence interaction, representing the tensor scalar product of scalar gradient, and the other accounts for the turbulent strain rate. Using eigenvalue decomposition, the term denoting scalar–turbulence interaction can be written as (Kolla *et al.* 2009)

$$\text{scalar}-\text{turbulence interaction} = -2\,\overline{\chi\,(e_\alpha \cos^2\alpha + e_\beta \cos^2\beta + e_\gamma \cos^2\gamma)}, \tag{1.4}$$

with e_α, e_β and e_γ being the turbulent strain tensor $\partial u_j'/\partial x_k$ eigenvalues. The three values satisfy the condition $e_\alpha > e_\beta > e_\gamma$, with e_α as the most extensive principal strain rate, and e_γ as the most compressive one. Relative orientation of the eigenvector corresponding to the e_α strain rate is given by α. It follows that the scalar–turbulence interaction acts as a source or sink, depending on predominant alignment of eigenvectors with the scalar gradient. Ashurst *et al.* (1987) pointed out that in turbulent flows, the scalar gradient has a preference to align with the most compressive principal strain rate, giving this term as a source. As for the other dominant term, which represents the stretching of the scalar field due to its local curvature, this has been related with the characteristic radius of iso-ξ surfaces (Mantel & Borghi 1994).

2. Numerical approach and set-up

The compressible solver HiPSTAR (Sandberg 2013) is used for the present DNS. HiPSTAR is a highly optimised hybrid MPI/OpenMP solver, used in numerous studies, covering turbulence (Sandberg *et al.* 2012; Bechlars & Sandberg 2017; Shin *et al.* 2017 ; Saini & Sandberg 2020), turbulent mixing (Shin *et al.* 2017*b*; Zhao & Sandberg 2021) and turbulent flow acoustics (Deuse & Sandberg 2020).

The code uses a structured, multi-block, curvilinear configuration, solving for the governing equations in cylindrical coordinates, thus allowing for an efficient distribution of grid points. Numerical schemes include a fourth-order finite-difference scheme in the streamwise and radial directions, along with a spectral method, based on Fourier decomposition in the azimuthal direction. Coordinate mapping is done in only two dimensions, allowing for a reduced number of metric terms. An axis treatment is applied, using parity conditions (Sandberg 2011). For improved numerical stability, skew-splitting of convective terms is applied (Kennedy & Gruber 2008). An explicit 11-points filter is applied in all flow directions, with filter weight 0.2, to dampen spurious oscillations (Bogey *et al.* 2009). An explicit, low-memory, fourth-order, five stages, explicit Runge–Kutta scheme is used for time marching (Kennedy *et al.* 2000). In addition to the flow governing equations, the conservation equation for a passive scalar is also solved for (see (1) in Aparece-Scutariu & Shin 2022).

The present DNS consist of a round turbulent air jet, issued into ambient air, without coflow, from a flat plate at Reynolds number $Re = 7290$). We define $Re = U_0 D/\nu$, where U_0 is the inlet velocity, D is the inlet diameter, and ν represents kinematic viscosity. The flow Mach number is subsonic at 0.304. The flow domain is stretched in the axial direction, spanning $55D$, with $30D$ in the radial direction. At the jet nozzle, the inflow condition is imposed with a top-hat mean velocity profile and weak turbulent fluctuations using a digital filter (Klein *et al.* 2003). A Navier–Stokes non-reflecting characteristic boundary condition (Kim & Lee 2000) is used at the streamwise outflow, with a zonal boundary (Sandberg & Sandham 2006) of 15 points, applied in the outlet vicinity, to dampen any

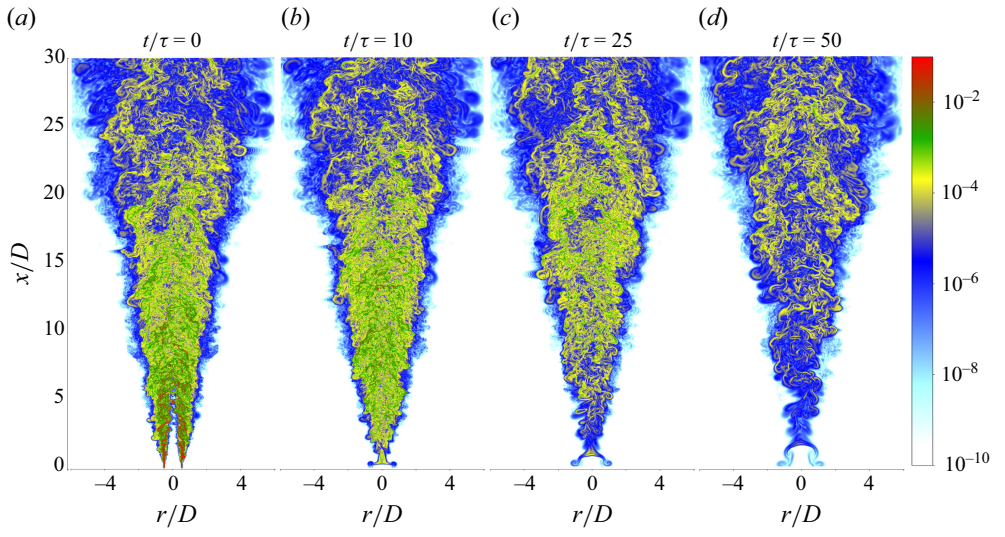

Figure 4. Non-dimensional instantaneous SDR in (*a*) the steady-state jet, and the stopping jet at times after stopping (*b*) 10τ, (*c*) 25τ, (*d*) 50τ.

unphysical reflections going back into the domain. In the azimuthal direction, a periodic boundary condition is used. Note that the domain of interest in the present study has length only $30D$ in the axial direction (figure 4). The remaining $25D$ serves as a safety distance, to reduce the possibility of the outlet exerting an influence on the flow field. The grid independence of the flow solution for the present DNS was previously demonstrated (see figure 1 of Shin *et al.* 2017*b*), with evidence of well-resolved SDR (see figure 3 of Aparece-Scutariu & Shin 2022).

Initially, the simulation runs from the quiescent flow field until a statistically stationary flow is established. Stationarity is demonstrated by the evolution of flow quantities, as shown by Shin *et al.* (2017*b*) and Aparece-Scutariu & Shin (2022). Then the inlet velocity is suddenly set to zero, resetting the time to $t = 0$. From the stopping point, one realisation is simulated until $t = 69\tau$, where τ is the characteristic jet time, defined as $\tau = D/U_0$. Note that 10 statistically independent realisations are produced for ensemble averaging. Due to the limited number of only 10 stopping jet instances, data were filtered for any noise using a one-dimensional Savitzky–Golay filter, based on local second-order polynomial fits over sets of points with fixed width (Guest 2012). Figure 4(*a–d*) show the instantaneous non-dimensional SDR field from one realisation, at different times after the point of stopping ($t/\tau = 0$).

3. Results

This section is structured as follows. First, a theoretical analysis assuming self-similarity is presented. The theoretical analysis provides relationships between self-similar variables, including an explicit relationship for $\overline{v'\chi'}$, which serves as a validation of the theoretical development. Subsequently, self-similarity characteristics of the stopping jet are presented through subsections covering evolution of the centreline profiles, radial profiles of individual terms of the transport equation, and the budget terms. Then the radial profile of $\overline{v'\chi'}$ is compared against the derived relationship in the theoretical subsection. Finally, existing algebraic models of the SDR-related terms are compared with DNS data, proposing suitable model coefficients and modifications.

3.1. *Theoretical analysis assuming self-similarity*

In this subsection, a theoretical analysis on the mean SDR is developed, using the assumption that flow variables remain self-similar in the unsteady jet. The assumptions of self-similarity will be thoroughly checked by DNS data in §§ 3.3 and 3.4. Furthermore, obtained theoretical predictions will be validated in § 3.5.

The analysis starts from the transport equation for the mean SDR in the case of an incompressible jet with constant mass diffusivity $\mathfrak{D}$:

$$\frac{\partial \overline{\chi}}{\partial t}+\frac{\partial \overline{u_j}\ \overline{\chi}}{\partial x_j}=\mathfrak{D}\frac{\partial^2\overline{\chi}}{\partial x_j\partial x_j}-\frac{\partial \overline{u_j'\chi'}}{\partial x_j}-4\mathfrak{D}\overline{\frac{\partial\xi}{\partial x_j}\frac{\partial u_j}{\partial x_i}\frac{\partial\xi}{\partial x_i}}-4\mathfrak{D}^2\overline{\frac{\partial^2\xi}{\partial x_j\partial x_i}\frac{\partial^2\xi}{\partial x_j\partial x_i}}. \tag{3.1}$$

Next, assuming that all involved variables are self-similar, the scaled ensemble-averaged statistics can be represented by a scaled radius $\eta=r/(x-x_0)$, where x_0 represents the jet virtual origin. Flow variables can be normalised by centreline values as

$$\begin{gathered}\overline{\chi}=\overline{\chi}_c g_\chi(\eta),\quad \overline{u}=\overline{u}_c g_u(\eta),\quad \overline{v}=\overline{u}_c g_v(\eta),\\ \overline{u'\chi'}=\overline{u}_c\,\overline{\chi}_c\,g_{u'\chi'}(\eta),\quad \overline{v'\chi'}=\overline{u}_c\,\overline{\chi}_c\,g_{v'\chi'}(\eta),\\ 4\mathfrak{D}^2\overline{\frac{\partial^2\xi}{\partial x_j\,\partial x_k}\frac{\partial^2\xi}{\partial x_j\,\partial x_k}}=\frac{\overline{u}_c\,\overline{\chi}_c}{r_{1/2}}h(\eta),\\ 4\mathfrak{D}\overline{\frac{\partial\xi}{\partial x_j}\frac{\partial u_j}{\partial x_k}\frac{\partial\xi}{\partial x_k}}=\frac{\overline{u}_c\,\overline{\chi}_c}{r_{1/2}}l(\eta),\end{gathered} \tag{3.2}$$

where g_χ, g_u, g_v, $g_{u'\chi'}$, $g_{v'\chi'}$, h and l are dimensionless shape functions characterising the self-similar profiles, respectively. Note that $r_{1/2}$ is the so-called half-radius, i.e. the radial location where axial velocity is half of the centreline axial velocity. Centreline variables $\overline{u}_c$ and $\overline{\chi}_c$ are functions of η and t. In previous studies of the stopping jet, $\overline{u}_c$ and $r_{1/2}$ are characterised as (Shin *et al.* 2017; Pope 2000)

$$\begin{aligned}\overline{u}_c&=C_u\frac{x-x_0}{t-t_0},\\ r_{1/2}&=S(x-x_0),\end{aligned} \tag{3.3}$$

where t_0 is a time shift, and C_u and S are some constants.

Substituting the relations in (3.2) and (3.3) into (3.1) results in

$$\begin{aligned}\frac{g_\chi}{C_u}\frac{t-t_0}{\overline{\chi}_c}\frac{\partial\overline{\chi}_c}{\partial t}+\left(g_u g_\chi+g_{u'\chi'}\right)\frac{x-x_0}{\overline{\chi}_c}\frac{\partial\overline{\chi}_c}{\partial x}&=\eta g_u\frac{\mathrm{d}g_\chi}{\mathrm{d}\eta}-g_v\frac{\mathrm{d}g_\chi}{\mathrm{d}\eta}-\frac{1}{\eta}\frac{\mathrm{d}\left(\eta g_{v'\chi'}\right)}{\mathrm{d}\eta}\\ &\quad+\eta\frac{\mathrm{d}g_{u'\chi'}}{\mathrm{d}\eta}-g_{u'\chi'}-\frac{1}{S}(h+l).\end{aligned} \tag{3.4}$$

The terms on the right-hand side of (3.4) are functions of η only, while the terms on the left-hand side are functions of x and t. In order for equality to hold, $\overline{\chi}_c$ only accepts a power-law form as

$$\overline{\chi}_c(x,t)=C_X(x-x_0)^a(t-t_0)^b, \tag{3.5}$$

where C_X is a constant. The power-law exponents a and b cannot be determined any further in this analysis. In Shin *et al.* (2017), power-law exponents of $\overline{u}_c$ for a stopping jet were determined explicitly using a similar approach. However, the difference is that velocity is nonlinear in its governing equation (momentum equation), while $\overline{\chi}$ is linear in its governing equation (see (3.1)).

It will be shown in § 3.2 that present DNS data indicate $a = 1$ and $b = -2$ as a good fit for $\overline{\chi}_c$ evolution, giving

$$\overline{\chi}_c(x, t) = \frac{C_{\overline{\chi}_c}}{U_0} \frac{x - x_0}{(t - t_0)^2}, \tag{3.6}$$

where a division by U_0 is included to match dimensions. Then substitution of (3.6) into (3.4) gives

$$-\frac{2}{C_u} g_\chi + g_u g_\chi - \eta g_u \frac{\mathrm{d}g_\chi}{\mathrm{d}\eta} + g_v \frac{\mathrm{d}g_\chi}{\mathrm{d}\eta} = -\left[\frac{g_{v'\chi'}}{\eta} + \frac{\mathrm{d}g_{v'\chi'}}{\mathrm{d}\eta}\right] - \left[2g_{u'\chi'} - \eta \frac{\mathrm{d}g_{u'\chi'}}{\mathrm{d}\eta}\right] - \frac{1}{S}(h + l). \tag{3.7}$$

Note that $C_{\overline{\chi}_c}$ does not appear in (3.7), due to linear dependency of $\overline{\chi}$ in the SDR transport equation (see (3.1)). At $\eta = 0$, the following relationships hold due to definitions and symmetry:

$$g_u(0) = 1, \quad g_v(0) = 0, \quad g_\chi(0) = 1, \quad g_{v'\chi'} = 0. \tag{3.8}$$

With the above relationships, evaluating (3.7) at $\eta = 0$ gives

$$\left[\frac{\mathrm{d}g_{v'\chi'}}{\mathrm{d}\eta}\right]_{\eta=0} = \frac{1}{C_u} - \frac{1}{2} - g_{u'\chi'}(0) - \frac{1}{2S}\big[h(0) + l(0)\big]. \tag{3.9}$$

Next, (3.7) can be integrated to obtain an explicit expression for $g_{v'\chi'}$ as

$$g_{v'\chi'} = \frac{2}{\eta C_u} \int_0^\eta \eta' g_\chi \, \mathrm{d}\eta' - \frac{4}{\eta} \int_0^\eta \eta' g_u g_\chi \, \mathrm{d}\eta' + \frac{3g_\chi}{\eta} \int_0^\eta \eta' g_u \, \mathrm{d}\eta' + \eta g_{u'\chi'} - \frac{4}{\eta} \int_0^\eta \eta' g_{u'\chi'} \, \mathrm{d}\eta' - \frac{1}{\eta S} \int_0^\eta \eta'(h + l) \, \mathrm{d}\eta'. \tag{3.10}$$

The two explicit expressions of (3.9) and (3.10) are compared with simulation data in § 3.5.

3.2. *Centreline SDR*

In this subsection, centreline SDR ($\overline{\chi}_c$) of the stopping jet is characterised using DNS. As shown in (3.2), centreline characteristics are the starting point of the self-similar analysis. The theoretical analysis in § 3.1 has not reached a conclusion on spatial and temporal dependencies. This will be solved in this subsection (see the paragraph after (3.5)).

Figure 5 shows the spatial and temporal evolution of $\overline{\chi}_c$ after stopping. Thin coloured lines represent ensemble-averaged $\overline{\chi}_c$ – note that ensemble averaging was done over 10 realisations. Profiles are normalised by the characteristic jet time $\tau = D/U_0$, with D and U_0 as the source diameter and velocity, respectively. The jet virtual origin $x_0 = 2.39D$ remains the same as for the steady-state jet (Shin *et al.* 2017*b*). For reference, the steady-state $\overline{\chi}_c$ is added as a thick black line. Overall, $\overline{\chi}_c$ decreases from its steady-state profile after stopping.

In the inlet vicinity ($x/D \approx 0$), centreline SDR momentarily increases immediately after stopping, then slowly decreases again to zero. The region corresponds to the potential core so that $\overline{\chi}_c$ is zero in the steady-state jet (see figure 4*a*). After the jet is stopped, the potential core collapses inwards, and SDR in the nozzle vicinity is no longer zero (see figure 4*b*). As time advances, SDR approaches to zero, as seen in figure 4(*c*,*d*).

Further downstream, after a peak, $\overline{\chi}_c$ evolves in the same way as for the steady-state profile. Behaviour is also similar to the observations of decelerating diesel jets

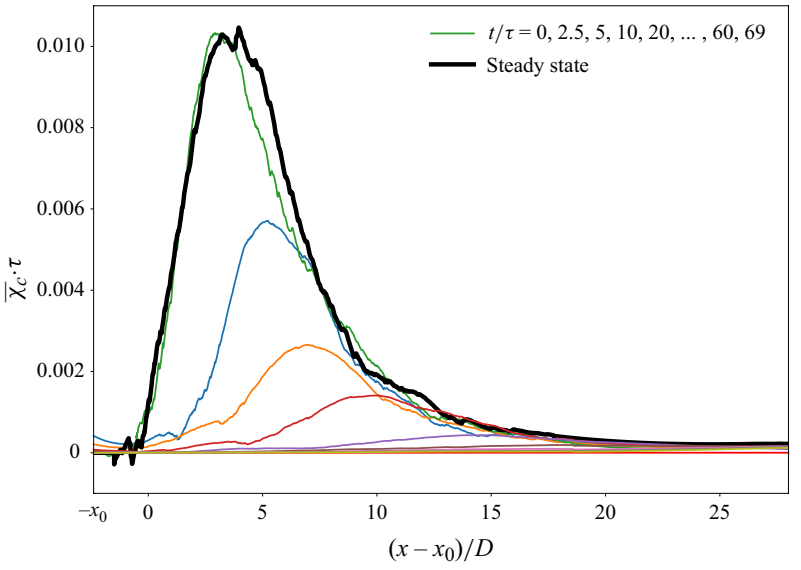

Figure 5. Centreline SDR variation with axial distance at multiple time instances.

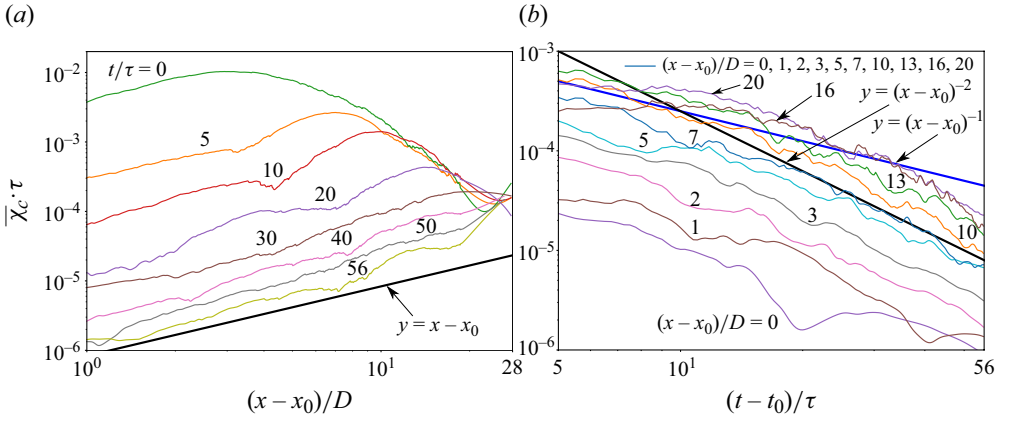

Figure 6. (*a*) The parabolic regime and (*b*) the inverse of $\overline{\chi}_c$ slope behaviour near the nozzle.

(Musculus 2009). After stopping, the decelerating wave propagates downstream with a certain speed. At locations where the decelerating wave has not arrived, $\overline{\chi}_c$ remains the same as in the steady-state jet. Similarity with the steady-state profile can also be seen in the instantaneous images of figure 4 – the instantaneous SDR characteristics after $x/D > 25$ remain similar for $t/\tau = 0{-}50$.

Long-term behaviour of the intermediate region between the nozzle inlet and the peak of $\overline{\chi}_c$ (e.g. $1 < (x - x_0)/D < 7$ at $t/\tau = 5$) will be analysed further.

Figures 6(*a*) and 6(*b*) replotted centreline SDR in two different ways to investigate spatial and temporal dependencies on the intermediate region. Figure 6(*a*) shows $\overline{\chi}_c$ in the log-log scale, with the x-axis being the axial distance with $1 < (x - x_0)/D < 12$. For reference, $y = x$ is added as a thick black line. As time advances, $\overline{\chi}_c$ becomes parallel to the black line, indicating that $\overline{\chi}_c$ becomes linear in x. Similarly, figure 6(*b*) shows $\overline{\chi}_c$ in the log-log scale with the x-axis being the time with $5 < (t - \tau_0)/\tau < 56$. For reference, $y = x^{-1}$ and $y = x^{-2}$ are added as thick blue and black lines. In the long time and in

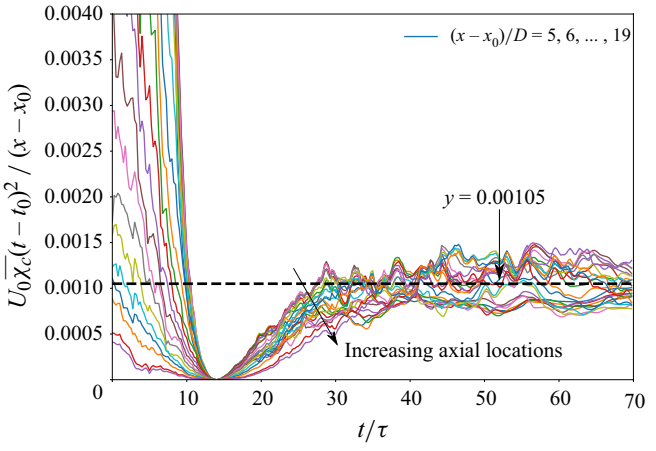

Figure 7. Scaled centreline SDR with time and axial distance at different axial locations.

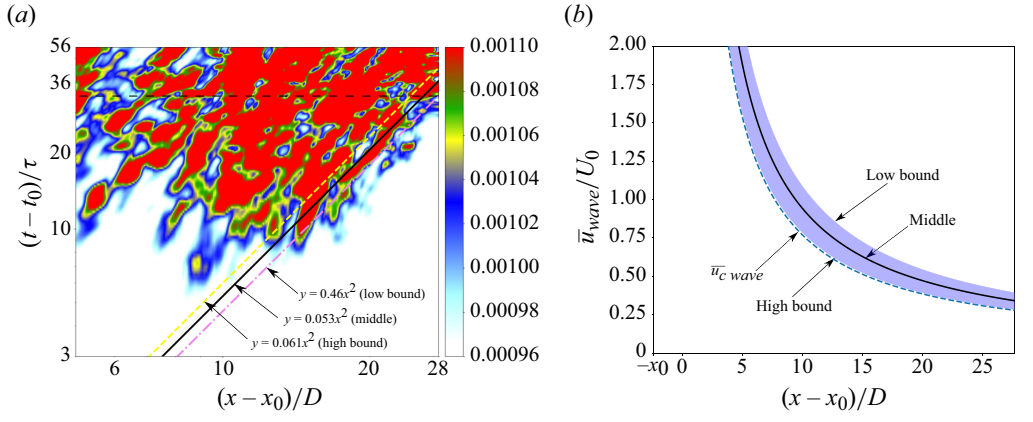

Figure 8. (*a*) False colours of $\overline{\chi}_c U_0(t-t_0)^2/(x-x_0)$, and (*b*) deceleration wave speed ($\overline{u}_{wave}$) for $\overline{\chi}_c$, along with evolution of centreline axial velocity $\overline{u}_c$.

the far field, $\overline{\chi}_c$ becomes parallel to the black line, meaning that $\overline{\chi}_c$ asymptotes to a $[(t-t_0)/\tau]^{-2}$ dependency. The analysis indicates that exponents in (3.5) are $a = 1$ and $b = -2$, respectively. The long term behaviour of $\overline{\chi}_c$ in the intermediate regime can be expressed as

$$\overline{\chi}_c = \frac{C_{\overline{\chi}_c}}{U_0}\frac{x-x_0}{(t-t_0)^2}, \tag{3.11}$$

where $C_{\overline{\chi}_c}$ is a dimensionless coefficient whose value will be evaluated, and U_0 is included to match the dimension.

Figure 7 shows scaled $\overline{\chi}_c$ over time to reconfirm spatial and temporal dependencies – the centreline SDR is scaled by $(x-x_0)/U_0(t-t_0)^2$. Again, the scaled $\overline{\chi}_c$ asymptotes to a constant in the long term. Scatter around the asymptotic value remains low, compared to the magnitude of early ($t/\tau < 14$) scaled profiles. The asymptotic constant $C_{\overline{\chi}_c}$ is 0.00105, as shown by the dashed line.

Next, the decelerating wave for the SDR is analysed. To quantify the decelerating wave, figure 8(*a*) shows the false colour of $\overline{\chi}_c U_0(t-t_0)^2/(x-x_0)$, using log scales. The false

colour displays a boundary separating two regions, one in red and the other in white. The boundary is not distinctive, but rather smooth with some width. Still, the boundary is clearly parallel to $y = x^2$. Hence this is treated as a characteristic line and drawn on the figure with a functional form as

$$\frac{t - t_0}{\tau} = \frac{1}{2C_{wave,SDR}} \left(\frac{x - x_0}{D} \right)^2. \tag{3.12}$$

As the boundary is not very distinctive, three candidates for $1/(2C_{wave,SDR})$ are selected, representing high, medium and low bounds with values 0.061, 0.053 and 0.046, respectively. Hence $C_{wave,SDR}$ takes values 8.2, 9.43 and 10.87, respectively. By the method of characteristics, the characteristic line in (3.12) should be a solution of the characteristic equation

$$\frac{\mathrm{d}x}{\mathrm{d}t} = u_{wave,SDR}. \tag{3.13}$$

With (3.12), $u_{wave,SDR}$ satisfies

$$\frac{u_{wave,SDR}}{U_0} = \frac{C_{wave,SDR}}{(x - x_0)/D}. \tag{3.14}$$

The $1/x$ dependency of $u_{wave,SDR}$ indicates that the SDR deceleration wave has a behaviour similar to that of the deceleration wave for axial velocity ($\overline{u}_c$) in the stopping jet (Shin *et al.* 2017), which is

$$\frac{u_{wave,velocity}}{U_0} = \frac{7.71}{(x - x_0)/D}. \tag{3.15}$$

For comparison, figure 8(*b*) shows the decelerating wave speeds for centreline SDR and axial velocity. This indicates that overall, the deceleration wave speed for SDR is slightly higher than for axial velocity. A quantitative comparison between the SDR wave speed and centreline axial velocity indicates that the former is between 1.06 and 1.41 times higher for the high and low bounds in figure 8(*b*), respectively.

Figure 8(*a*) can also be used to set the ranges, where the long-term asymptotic behaviour is observed. The horizontal black dashed line is the line $(t - \tau_0)/\tau = 36$, which crosses the decelerating wave line (black solid line) at $(x - x_0)/D = 26$. Considering $x_0 = 2.39D$ and $t_0 = 14\tau$, the ranges $14 < x/D < 28$ and $50 < t/\tau < 69$ can be used to obtain statistics for long-term behaviour analysis.

3.3. *Self-similarity of the mean SDR in a stopping jet*

This subsection analyses radial profiles of the mean SDR and its axial, radial and azimuthal components. As shown in § 3.2, scaled centreline SDR $\overline{\chi}_c U_0 (t - t_0)^2/(x - x_0)$ asymptotes to a constant value, after some transient time. Based on this behaviour, the current subsection focuses on identifying new self-similar states in the stopping jet. In the first subsubsection, stationarity and homogeneity of normalised radial profiles of the SDR are investigated. The second subsubsection presents new self-similar states, which are different from their steady-state counterparts.

3.3.1. *Stationarity and homogeneity of the SDR radial profiles*

Stationarity of SDR and its components is first checked at selected axial locations $(x - x_0)/D = 14$ and 28. Figure 9 shows radial profiles of axial, radial, azimuthal and the total SDR components, at different times after the jet is stopped. Profiles are normalised

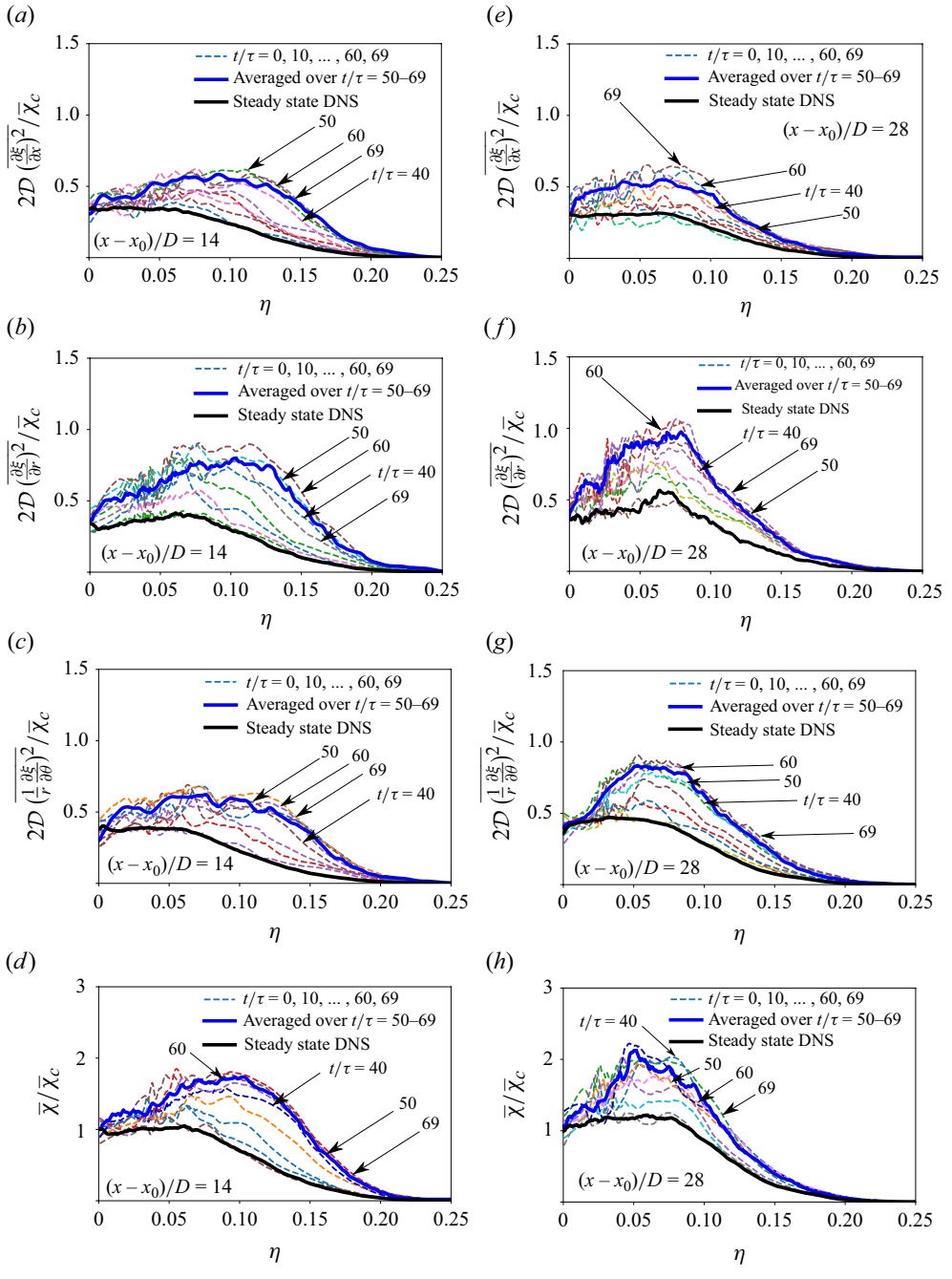

Figure 9. Normalised radial profiles of transient axial SDR component at (a) $(x - x_0)/D = 14$ and (e) $(x - x_0)/D = 28$, radial SDR component at (b) $(x - x_0)/D = 14$ and (f) $(x - x_0)/D = 28$, azimuthal SDR component at (c) $(x - x_0)/D = 14$ and (g) $(x - x_0)/D = 28$, total SDR at (d) $(x - x_0)/D = 14$ and (h) $(x - x_0)/D = 28$.

by centreline SDR ($\overline{\chi}_c$). On each plot, the blue thick line represents averaged profile over $t/\tau = 50$–69 to be termed hereafter 'long-term profiles'. As seen in figure 8(*a*), the decelerating wave passes by at approximately $t/\tau = 24$ and 35 for $(x - x_0)/D = 14$ and

28, respectively. Hence the time range $t/\tau = 50{-}69$ falls into the interval where long-term behaviour can be observed at both locations.

Overall, transient profiles increase over time. As time advances, profiles start near the steady-state profiles (black lines), and slowly move to long-term profiles (blue lines), then settle down at the long-term profiles.

Figures 9(*a*) and 9(*e*) show the normalised axial SDR components. The long-term profiles are higher than their steady-state counterparts. At both axial locations, long-term profiles slightly increase with η, from the centreline towards a peak, and then decay to zero further away from the centreline. Figures 9(*b*) and 9(*f*) show the normalised radial SDR components. The long-term profiles show the highest increase in magnitude, compared to the steady-state profiles. The increase is mostly visible at $(x - x_0)/D = 28$, which also shows the highest peak dissipation at $\eta \approx 0.09$, approximately 2.5 times higher than the centreline value. Figures 9(*c*) and 9(*g*) show the azimuthal SDR component. Long-term profiles resemble those of the axial component, which is also the case for the steady-state jet. At $(x - x_0)/D = 14$, the long-term profile is relatively flat, whereas at $(x - x_0)/D = 28$, there is a distinct peak in dissipation at $\eta \approx 0.07$.

Finally, figures 9(*d*) and 9(*h*) show the total SDR long-term profiles. Again, the long-term profiles are higher than the steady-state profiles, with the largest contribution from the radial component. Also, on all figures, the instantaneous profiles of $t/\tau = 50, 60, 69$ are all around the long-term profiles, which confirms stationarity in the inspected time range. Furthermore, total SDR goes to zero at the same η location for both steady-state and long-term profiles. This indicates that the jet spreading angle does not change while the jet is decelerating.

3.3.2. *Homogeneity of the SDR radial profiles*

Next, homogeneity of profiles is investigated. Figures 10(*a–d*) show long-term radial profiles (i.e. averaged over $t/\tau = 50{-}69$) of the SDR and its components at axial locations $(x - x_0)/D = 14{-}28$. At each axial location of the given range, stationarity is observed at the inspected times, as shown in figure 9. Overall, there is some degree of scatter among the lines in all figures. The scatter would be attributed to limited simulation data – the ensemble averaging uses 10 azimuthally averaged realisations. Still, the small scatter indicates that long-term profiles are homogeneous after the passage of the decelerating wave.

Among the SDR components, overall shapes and magnitudes are similar to each other. Similarity indicates that the mean SDR is isotropic, hence the total SDR can be inferred from one component of the SDR. The $\overline{\chi}/\overline{\chi}_c$ radial profile increases approximately 1.5 times the centreline value, until $\eta \approx 0.1$, followed by a decay to zero until $\eta = 0.25$.

So far, stationarity and homogeneity were evaluated for the time interval $t/\tau = 50{-}69$ and over the axial distance $(x - x_0)/D = 14{-}28$. The choices of the ranges for x and t are imposed by nozzle proximity, available simulation time and speed of the deceleration wave. The ranges fall inside the regime in which the centreline SDR reaches an asymptotic state (figure 6). Hence chosen ranges of x and t intervals are wide enough to highlight universality of radial profiles, with a ratio for axial locations calculated based on $x - x_0 = 15$ and time span 19τ.

Figures 10(*e–h*) show spatially averaged long-term profiles of the total SDR and its three components, to be termed hereafter ‘decelerating self-similar profiles’. Decelerating self-similar profiles in the blue thick lines are obtained by averaging the long-term profiles over $t/\tau = 50{-}69$ and $(x - x_0)/D = 14{-}28$. Black thick lines are the steady-state self-similar profiles. The shaded region represents an error bound of one standard deviation (S.D.).

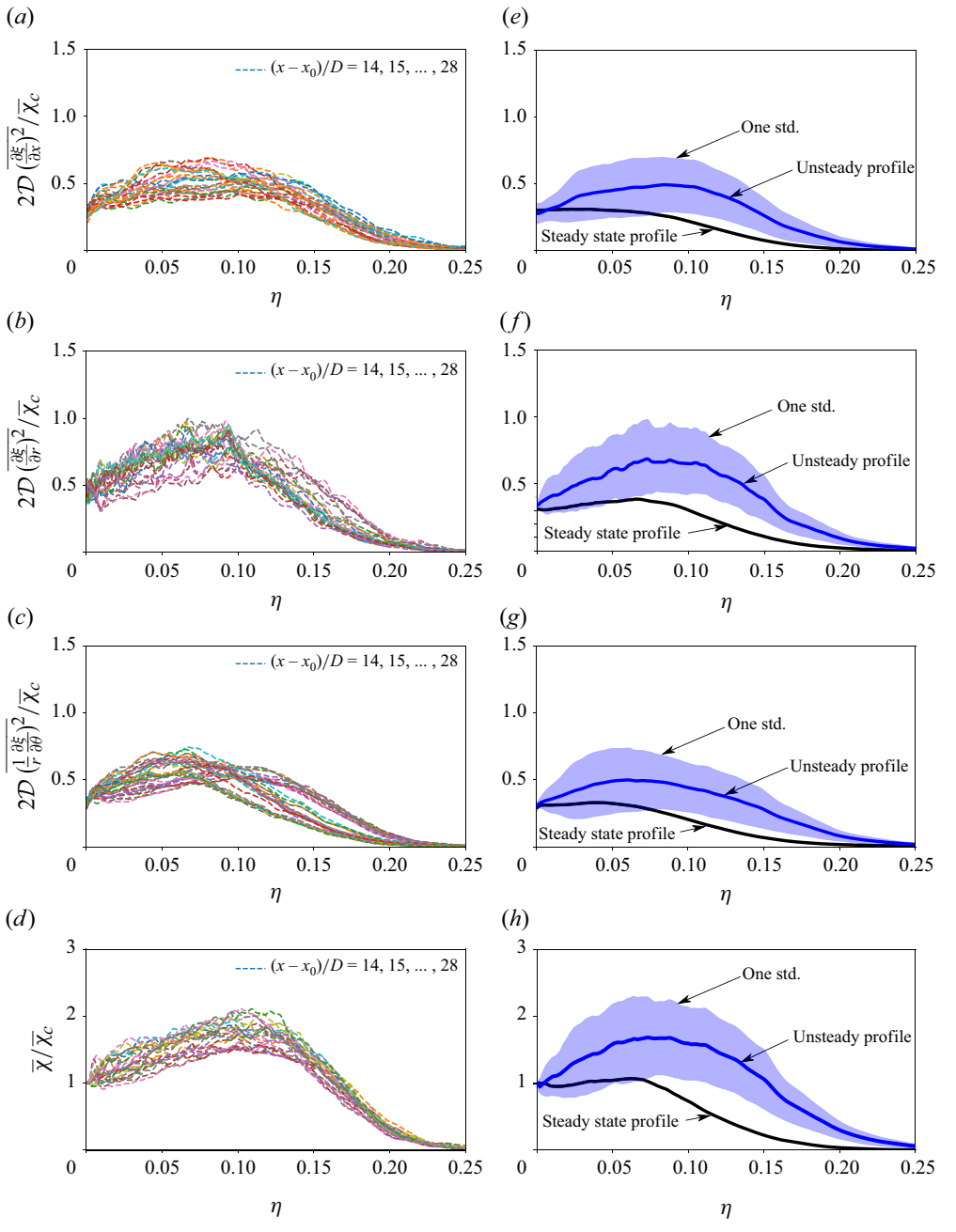

Figure 10. Temporally averaged profiles of normalised SDR components (*a*) axial, (*b*) radial and (*c*) azimuthal as well as (*d*) total SDR at $(x - x_0)/D = 14{-}28$; and self-similar profiles averaged over $t/\tau = 50{-}69$ and $(x - x_0)/D = 14{-}28$ for SDR components (*e*) axial, (*f*) radial and (*g*) azimuthal as well as (*h*) total SDR.

For the axial SDR component (figure 10*e*), the profile is momentarily lower than its steady-state equivalent in the centreline vicinity. However, away from the centreline it increases, peaking at $\eta \approx 0.10$ with approximately 1.5 times the centreline value. The radial SDR component (figure 10*f*) remains more intense than its steady-state counterpart along the entire radial direction, showing the steepest increase among the

SDR components. The peak occurs at $\eta \approx 0.08$, whose value is approximately 1.6 times the centreline value. The azimuthal SDR component (figure 10*g*) is again higher than its steady-state equivalent. The peak occurs at $\eta \approx 0.08$, with a value approximately 1.3 times higher than the magnitude at the centreline. The decelerating self-similar profile of the total SDR (figure 10*h*) remains higher than its steady-state counterpart along the entire scaled radius. Monotonic increase of the decelerating self-similar profile peaks at $\eta \approx 0.08$ and is approximately 1.5 times higher than the centreline value.

3.4. *Self-similarity of the mean SDR transport equation in a stopping jet*

In previous subsections, the mean SDR in the stopping jet reaches new self-similar states after a transient time. These profiles are termed decelerating self-similar profiles. In this subsection, analysis is extended to the terms in the mean SDR transport equation (3.1). For ease of reading, this equation is rearranged so that all the terms are moved to the right-hand side, as follows:

$$0 = \underbrace{-\frac{\partial \overline{\chi}}{\partial t}}_{\mathrm{I}} \underbrace{-\frac{\partial \overline{u}_j\,\overline{\chi}}{\partial x_j}}_{\mathrm{II}} \underbrace{+\mathfrak{D}\frac{\partial^2 \overline{\chi}}{\partial x_j\,\partial x_j}}_{\mathrm{III}} \underbrace{-\frac{\partial \overline{u_j'\chi'}}{\partial x_j}}_{\mathrm{IV}} \underbrace{-4\mathfrak{D}\overline{\frac{\partial \xi}{\partial x_j}\frac{\partial u_j}{\partial x_i}\frac{\partial \xi}{\partial x_i}}}_{\mathrm{V}} \underbrace{-4\mathfrak{D}^2\overline{\frac{\partial^2 \xi}{\partial x_j\,\partial x_i}\frac{\partial^2 \xi}{\partial x_j\,\partial x_i}}}_{\mathrm{VI}}. \tag{3.16}$$

In addition, all the terms are defined by Roman numerals, which are used hereafter. Note that some definitions contain a minus sign and some do not. The inclusion or exclusion of a minus sign is consistent with previous studies (Mantel & Borghi 1994; Mura & Borghi 2003; Chakraborty *et al.* 2011).

A previous analysis of the mean SDR equation shows that as for the steady-state case (Aparece-Scutariu & Shin 2022), mean SDR convection (term II), mean SDR diffusion (term III) and turbulent transport (term IV) remain negligible. Hence the analysis focuses on the remaining significant terms (I, V, VI). Significance will be reconfirmed by evaluating balance in the last subsection. The analysis will be conducted in the same manner as the SDR analysis in the previous subsection. Stationarity and homogeneity for radial profiles are first analysed. Then decelerating self-similar profiles are presented.

Figure 11 shows normalised radial profiles of significant terms in (3.16) at axial locations $(x - x_0)/D = 19$ and 28. Terms are normalised by $(\overline{u}_c\,\overline{\chi}_c)/r_{1/2}$, as in § 3.1. In each plot, profiles are shown in time increments of 10τ after stopping. Blue thick lines represent averaged profiles over $t/\tau = 50{-}69$. The time interval is considered based on the scaled $\overline{\chi}_c$, which displays an asymptotic trend, beyond $t/\tau > 40$, at both axial locations (see figure 6*c*).

Figures 11(*a*) and 11(*d*) show the normalised temporal term of SDR (term I in (3.16)). At all times, the value remains negative, indicating that the mean SDR decreases over time. At $t/\tau > 50$, radial profiles remain close to the long-term profiles. While profiles of $x/D = 19$ and 28 are not identical, both show the same trend. Long-term profiles start at approximately -0.8 at the centreline, remain on a plateau, except for any spurious oscillations, and then, at approximately $\eta = 0.09$, the value goes to zero. As term I includes a derivative of SDR (i.e. higher-order statistics), spurious oscillations are unavoidable.

Figures 11(*b*) and 11(*e*) show terms associated with construction by the stretch of scalar field due to local curvature (term V in (3.16)) at the two axial locations $(x - x_0)/D = 19$ and 28. Again, the profiles are not exactly identical at the two locations, but they show similar trends. Over time, profiles transition from the steady-state profile to the long-term profile. After $t/\tau = 50$, the profile remains close to the long-term profile. The long-term

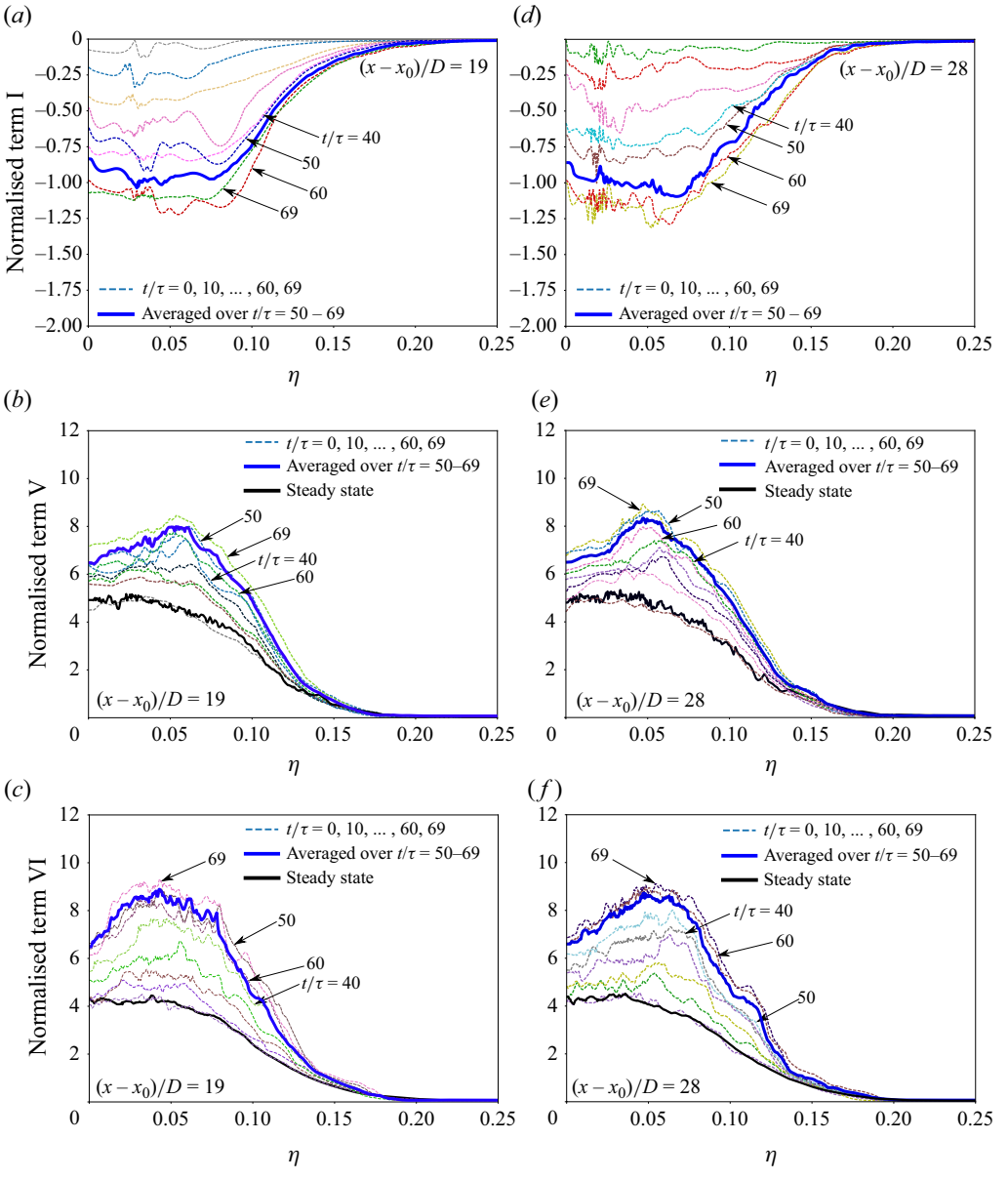

Figure 11. Transient behaviour of radial profiles for dominant budget terms in the mean SDR transport equation: term I at (*a*) $(x - x_0)/D = 19$ and (*d*) $(x - x_0)/D = 28$; term V at (*b*) $(x - x_0)/D = 19$ and (*e*) $(x - x_0)/D = 28$; and term VI at (*c*) $(x - x_0)/D = 19$ and (*f*) $(x - x_0)/D = 28$.

profile starts from approximately 6.5 at the centreline, and increases with η. Then it peaks at $\eta \approx 0.05$, followed by a decay to zero.

Figures 11(*c*) and 11(*f*) show the destruction term (term VI in (3.16)) at the two axial locations. At both locations, profiles transition again from the steady-state profile to the long-term profile, until $t/\tau = 50$. The long-term profile starts from 6.3 at the centreline, and decreases with η, reaching a negative peak at approximately $\eta = 0.07$, and then goes to zero. Overall, figure 11 illustrates that all dominant terms reach the long-term profiles at the two inspected locations after stopping, especially after $t/\tau > 50$.

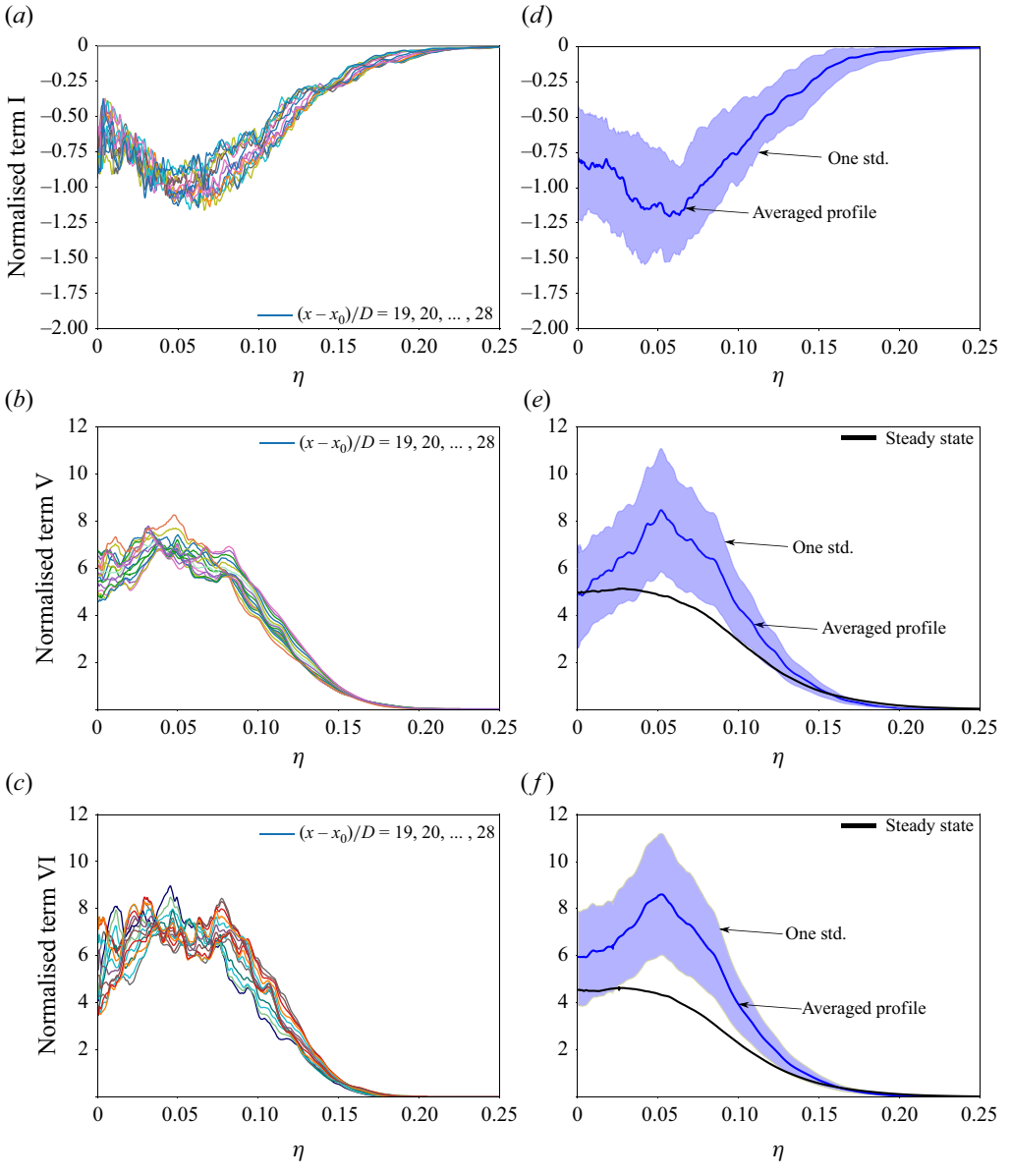

Figure 12. Temporally averaged dominant terms of the mean SDR transport equation for (*a*) term I, (*b*) term V and (*c*) term VI; and normalised radial profiles of (*d*) term I, (*e*) term V and (*f*) term VI, self-similar over $t/\tau = 50{-}69$ and $x/D = 19{-}28$.

Next, homogeneity of the long-term profiles is inspected. Figure 12(*a–c*) show the normalised radial profiles for the dominant terms in the axial range $(x - x_0)/D = 19{-}28$. Profiles are first averaged over the time interval $t/\tau = 50{-}69$ and then are normalised by $(\overline{u}_c\, \overline{\chi}_c)/r_{1/2}$. These centreline variables are also averaged over the time interval $t/\tau = 50{-}69$. Overall, variations among locations are small.

Then figure 12(*d–f*) show spatially averaged long-term profiles for the three dominant terms, denoted hereafter as decelerating self-similar profiles. The blue shaded region

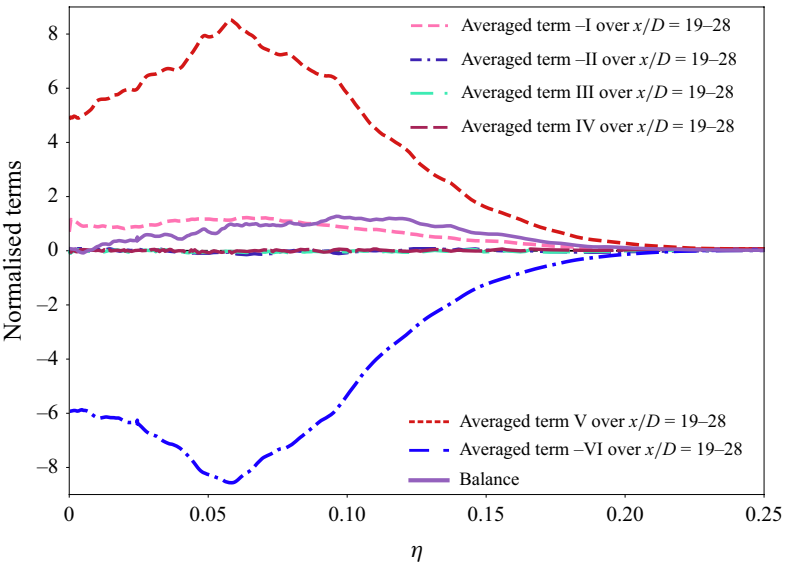

Figure 13. Balance of temporally and spatially averaged budget terms of the mean SDR transport equation (3.16).

indicates one standard deviation of the averaged profile, and the black line indicates its corresponding radially averaged steady-state profile.

Term I (the temporal term) starts from a negative value near the jet centreline, peaking at $\eta \approx 0.07$, followed by a monotonic increase to 0 until $\eta \approx 0.25$. As for terms V and VI (figure 12*d–f*), radial profiles are homogeneous in the interval $(x - x_0)/D = 19{-}28$. Term V (production term) has an off-centreline peak, followed by a decrease at outer radii. Term VI (destruction term) shows the same trend as the production term. In terms of order of magnitude, terms V and VI are approximately 5 times larger than term I. Hence terms V and VI balance the equation at leading order, although term I has a non-negligible influence on this balance.

Finally, figure 13 shows the balance of the mean SDR transport equation. The balance term considers all terms in (3.16), including the significant terms I, V and VI, as well as the negligible ones, II, III and IV. Balance is zero at the centreline, but becomes negative away from the jet axis. Note that the three significant terms still have a certain amount of uncertainty, as shown in figure 12(*d–f*). Hence variation of the balance term would be attributed to statistical uncertainty of the dominant terms. Still, the relatively small magnitude balance term validates the computation of the three significant terms, as they are introduced in the first part of this subsection. Overall, the biggest contributions are due to terms V and VI in (3.16). These are followed by the temporal term I, which is approximately 20 % in magnitude of either term V or term VI. Equation (3.16) is considered to be balanced, given the fact that the balance is overall smaller than relevant budget terms (i.e. terms I, V and VI).

3.5. *Prediction of the self-similar profile of $\overline{v'\chi'}$ in a stopping jet*

In § 3.1, the self-similar radial profile of $\overline{v'\chi'}$ and its derivative at $\eta = 0$ are given in (3.9) and (3.10). Derivation is based on the assumption of self-similarity of the other involved terms. Hence agreement of the derivation with actual DNS profiles can serve as indirect evidence of self-similarity occurring in the stopping jet.

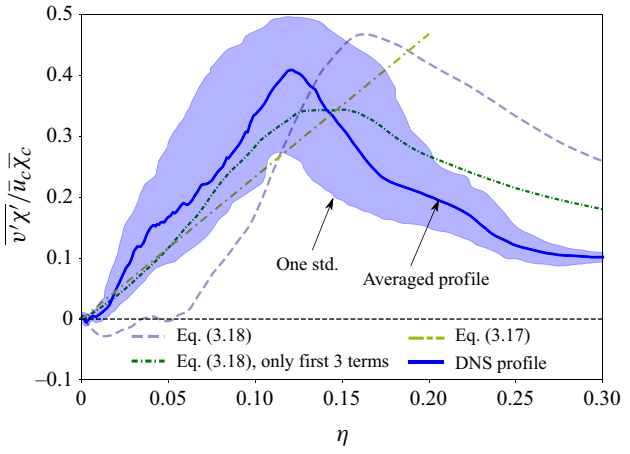

Figure 14. Normalised decelerating self-similar profiles over $t/\tau = 50{-}69$ and $(x - x_0)/D = 14{-}28$ for $\overline{v'\chi'}$.

For ease of reading, (3.9) and (3.10) are rewritten below:

$$\left[\frac{\mathrm{d}g_{v'\chi'}}{\mathrm{d}\eta}\right]_{\eta=0} = \frac{1}{C_u} - \frac{1}{2} - g_{u'\chi'}(0) - \frac{1}{2S}\big[h(0) + l(0)\big], \tag{3.17}$$

$$g_{v'\chi'} = \frac{2}{\eta C_u}\int_0^\eta \eta' g_\chi \,\mathrm{d}\eta' - \frac{4}{\eta}\int_0^\eta \eta' g_u g_\chi \,\mathrm{d}\eta' + \frac{3g_\chi}{\eta}\int_0^\eta \eta' g_u \,\mathrm{d}\eta' + \eta g_{u'\chi'} - \frac{4}{\eta}\int_0^\eta \eta' g_{u'\chi'} \,\mathrm{d}\eta' - \frac{1}{\eta S}\int_0^\eta \eta'(h + l)\,\mathrm{d}\eta'. \tag{3.18}$$

The derivations require profiles of

$$\overline{u},\ \overline{\chi},\ \overline{u'\chi'},\ 4\mathfrak{D}^2\overline{\frac{\partial^2\xi}{\partial x_j\partial x_i}\frac{\partial^2\xi}{\partial x_j\partial x_i}},\quad 4\mathfrak{D}\overline{\frac{\partial\xi}{\partial x_j}\frac{\partial u_j}{\partial x_i}\frac{\partial\xi}{\partial x_i}}. \tag{3.19}$$

The decelerating self-similar profile of $\overline{u'\chi'}$ is presented in Appendix A, while all the other profiles are presented in previous sections.

Figure 14 shows the decelerating self-similar profile of $\overline{v'\chi'}$ along with various predictions. Again, the shaded region indicates one standard deviation of the mean profile. The light green dot-dashed straight line is the predicted slope, using (3.9). The values $C_u = 0.441$ (Shin *et al.* 2017), $S = 0.085$ (i.e. jet spreading rate), $g_{\overline{u'\chi'}}(0) = -0.092$, $h(0) = -5.405$ and $l(0) = 5.642$ are assigned to the equation. The predicted slope (0.468) is close to the actual average slope of the averaged decelerating self-similar profile until $\eta \approx 0.11$ (0.353).

Predicted radial profiles based on (3.18) are plotted as dashed and dot-dashed lines. The purple dashed line includes all terms in (3.18), while the green dot-dashed line includes only the first three terms on the right-hand side. Prediction with only three terms shows better agreement with the actual averaged profile. If all terms are included, the prediction seems to be shifted rightwards to some extent. Note that the first three terms in (3.18) have a high level of confidence, as these are related to first-order statistics, while the remaining terms have a lower confidence level, due to their nature of higher-order statistics. Hence including the remaining terms would lead to undesirable uncertainty, due to their lower confidence level with regard to statistics.

Overall, proximity of slope and radial profile predictions increases the validity of self-similar behaviour of the SDR in the stopping jet.

3.6. *Scaling of turbulent modelling for terms in the $\overline{\chi}$ transport equation*

In this subsection, the existing turbulence models for the SDR are compared with DNS data, and additional modifications are proposed. For brevity, spatial and temporal virtual origins (x_0 and t_0) are omitted in this subsection.

Three algebraic models are found in the literature for SDR modelling. Libby & Bray (1980) proposed a model for mean SDR, relating turbulent energy dissipation (ϵ), turbulent kinetic energy (k) and mixture fraction variance ($\overline{\xi'^2}$), denoted the LB model:

$$\overline{\chi} = C_{LB}\frac{\epsilon}{k}\overline{\xi'^2}. \tag{3.20}$$

Mantel & Borghi (1994) proposed algebraic models for the two dominant terms in the SDR transport equation (3.16). Mantel & Borghi (1994) argued that as every term in (3.1) depends on the turbulent Reynolds number, in the large turbulent Reynolds number limit, the following models for dominant terms associated with scalar–turbulence interaction (term V in (3.16)) and effects of local curvature (term VI in (3.16)) can be developed. The model for term V, denoted the MB5 model, is

$$-4\mathfrak{D}\overline{\frac{\partial\xi}{\partial x_j}\frac{\partial\xi}{\partial x_i}\frac{\partial u_j}{\partial x_i}} = 2\alpha\frac{\epsilon}{k}\overline{\chi}, \tag{3.21}$$

and the model for term VI, denoted the MB6 model, is

$$4\mathfrak{D}^2\overline{\frac{\partial^2\xi}{\partial x_j\partial x_i}\frac{\partial^2\xi}{\partial x_j\partial x_i}} = 2\beta\frac{\overline{\chi}^2}{\overline{\xi'^2}}, \tag{3.22}$$

where α and β are dimensionless constants.

As shown in Aparece-Scutariu & Shin (2022) and in previous subsections, both steady-state and stopping jets show self-similar characteristics. Henceforth, the three models in (3.20)–(3.22) should be self-similar as well. At first glance, the models would seem to be self-similar, as constituent variables (ϵ, k, $\overline{\xi'^2}$, $\overline{\chi}$) are self-similar. Still, caution is necessary, as self-similarity requires normalisation by certain centreline values, which can be different from case to case. An alternative way to check self-similarity is to check if the x and t scalings of the models are the same as the targeted variables.

In the steady-state jet, $\overline{\chi}$ scales as $1/x^4$ (Aparece-Scutariu & Shin 2022). The constituent variables in the LB model are ϵ, k and $\overline{\xi'^2}$, which scale as $1/x^4$, $1/x^2$ and $1/x^2$, respectively. Then the collective scaling of the LB model without C_{LB} is $1/x^4$, which agrees with the scaling of $\overline{\chi}$ for the steady-state jet. The same analysis is done for the other two models. Table 1 summarises x and t scalings for each variable for the steady-state jet. The first two rows are the measured scaling from Aparece-Scutariu & Shin (2022). The next two rows show the scalings of the three algebraic models, without the modelling parameters. The three models agree with the x scalings of their target variables in the steady-state jet, so comparisons can be made by self-similar variables.

Figure 15 shows self-similar profiles of $\overline{\chi}$, term V, and term VI over the scaled radius. Note that the three profiles are normalised by $\overline{\chi}_c$, $(\overline{u_c}\,\overline{\chi_c})/r_{1/2}$ and $(\overline{u_c}\,\overline{\chi_c})/r_{1/2}$, respectively. In addition, the three algebraic models with optimal parameters are included.

Variable	k	$\overline{\xi'^2}$	ϵ	$\overline{\chi}$	Term V	Term VI
Scaling	$\frac{1}{x^2}$	$\frac{1}{x^2}$	$\frac{1}{x^4}$	$\frac{1}{x^4}$	$\frac{1}{x^6}$	$\frac{1}{x^6}$
Variable				LB model without C_{LB}	MB5 model without α	MB6 model without β
Scaling				$\frac{1}{x^4}$	$\frac{1}{x^6}$	$\frac{1}{x^6}$

Table 1. Spatial and temporal scalings of flow variables for the steady-state jet.

Variable	k	$\overline{\xi'^2}$	ϵ	$\overline{\chi}$	Term V	Term VI
Scaling	$\frac{x^2}{t^2}$	$\frac{x^2}{t^2}$	$\frac{x^2}{t^3}$	$\frac{x}{t^2}$	$\frac{x}{t^3}$	$\frac{x}{t^3}$
Variable				LB model without C_{LB}	MB5 model without α	MB6 model without β
Scaling				$\frac{x^2}{t^3}$	$\frac{x}{t^3}$	$\frac{1}{t^2}$

Table 2. Spatial and temporal scalings of flow variables for the stopping jet.

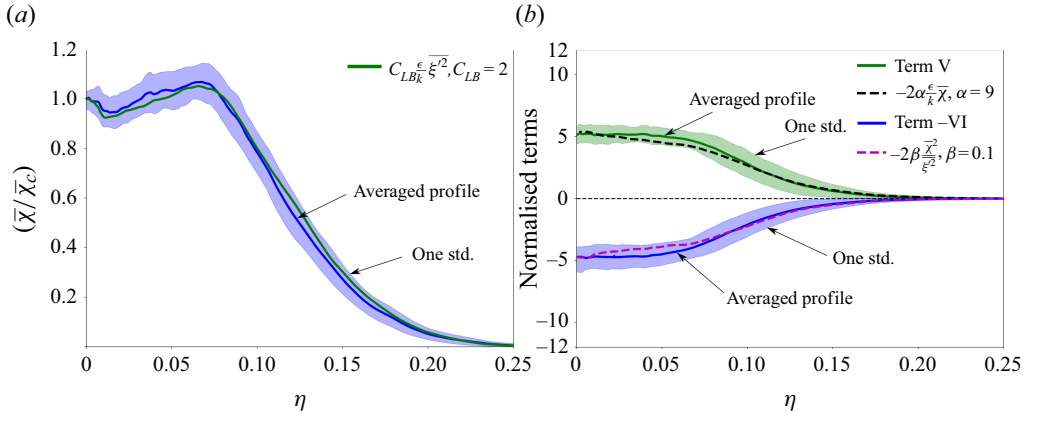

Figure 15. Comparison between the actual data and the algebraic models in the steady-state jet corresponding to (*a*) SDR and (*b*) terms V and VI from (3.1).

Radial profiles of the models agree well with actual data. The optimal parameters for the steady-state jet are

$$C_{LB} = 2, \quad \alpha = 9, \quad \beta = 0.1. \tag{3.23}$$

Note that previous works reported similar values of C_{LB}: 1.0 from Jones (1994), 2.0 from Janicka & Peters (1982), 2.0 from Overholt & Pope (1996), and 3.0 from Juneja & Pope (1996).

Next, the same scaling analysis is conducted for the stopping jet. Table 2 summarises the scalings of flow variables and the models. Again, the first two rows are the measured

Variable	l_t	u'	Re_t
Scaling for the steady-state jet	x	$\frac{1}{x}$	1
Scaling for the stopping jet	x	$\frac{x}{t}$	$\frac{x^2}{t}$

Table 3. Spatial and temporal scaling of the turbulent Reynolds number and its related variables.

scalings from Shin *et al.* (2017, 2023) and this work, and the next two rows show scalings of the three algebraic models without modelling parameters. The scaling of the MB5 model agrees with that of term V. However, the LB model without C_{LB}, and the MB6 model without β, do not match the targeted scalings.

A plausible fix for the scaling mismatch is to impose scalings on the modelling parameters. The necessary scalings are t/x for C_{LB}, and x/t for β. Mantel & Borghi (1994) applied a $Re_t^{1/2}$ scaling to β in the context of decaying homogeneous isotropic turbulence flow in order to match with their order of magnitude analysis. Hence a scaling with Re_t is tested for the model parameters C_{LB} and β.

Table 3 shows the scalings of the turbulent Reynolds number (Re_t) and its related variables, which are based on (Pope 2000)

$$Re_t = \frac{l_t u'}{\nu}, \quad \text{where } l_t = \frac{k^{3/2}}{\epsilon} \text{ and } u' = k^{1/2}. \tag{3.24}$$

Given table 3, two types of modifications are proposed, as follows. The first modification, denoted Type 1, is

$$C_{LB} = \frac{C_{LB,1}}{D}\frac{l_t}{Re_t}, \quad \beta = \beta_1 D \frac{Re_t}{l_t}. \tag{3.25}$$

The second modification, denoted Type 2, is

$$C_{LB} = C_{LB,2}\left(\frac{U_0}{D}\frac{l_t}{Re_t\, u'}\right)^{1/2}, \quad \beta = \beta_2\left(\frac{D}{U_0}\frac{Re_t\, u'}{l_t}\right)^{1/2}. \tag{3.26}$$

Note that l_t and u' have dimensions of length and velocity, so additional length/velocity scales (D and U_0) are added to keep the new parameters dimensionless. Type 1 has simpler expressions for C_{LB} and β. Type 2 includes a $Re_t^{1/2}$ scaling, which appears in the scaling of the two dominant terms in the SDR transport equation (Mantel & Borghi 1994; Mura & Borghi 2003).

By using the two types of modification, radial profiles can be predicted with self-similar variables. Figures 16 and 17 show a comparison of the normalised radial profiles for the models, over the scaled radius. The resulting optimal parameters are

$$\alpha = 42, \tag{3.27}$$

parameters for Type 1

$$C_{LB,1} = 70, \quad \beta_1 = 0.1, \tag{3.28}$$

and parameters for Type 2

$$C_{LB,2} = 3, \quad \beta_2 = 25. \tag{3.29}$$

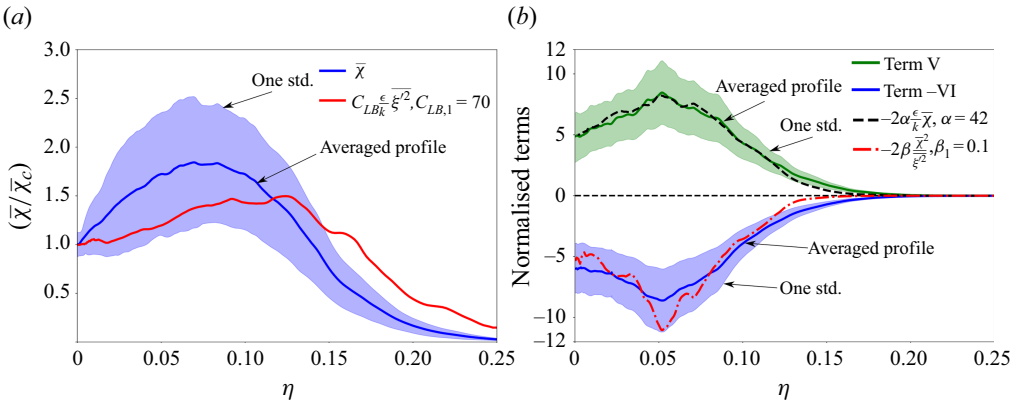

Figure 16. Comparison between the actual data and the algebraic models using Type 1 modification (3.25) in the stopping jet corresponding to (*a*) the SDR and (*b*) terms V and VI from (3.1).

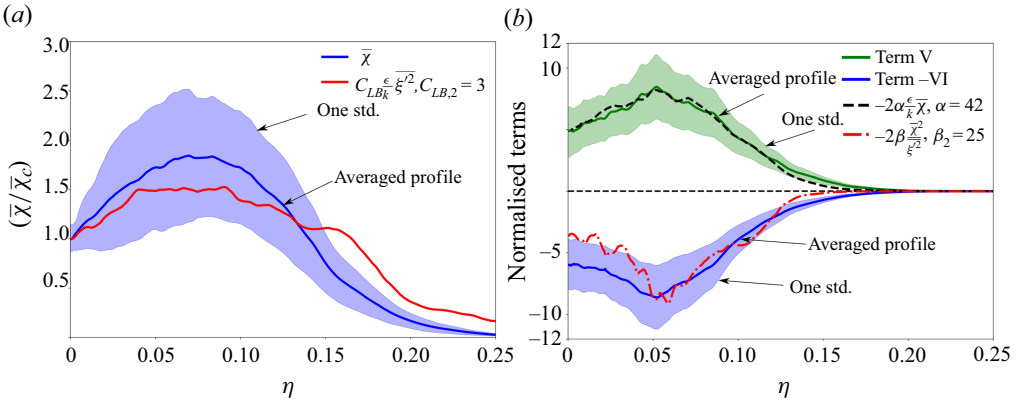

Figure 17. Comparison between the actual data and the algebraic models using Type 2 modification (3.26) in the stopping jet corresponding to (*a*) the SDR and (*b*) terms V and VI from (3.1).

For LB models, Type 2 modification seems to fit better with actual data. For the MB5 model, which does not need a modification, there is very good agreement with the actual data. For the MB6 model, both modifications produce results that fit within one standard deviation.

4. Conclusions

Spatio-temporal characteristics of turbulent mixing have been investigated in a stopping jet, using direct numerical simulations. Key investigated parameters are the ensemble-averaged scalar dissipation rate (SDR) and dominant terms in the mean SDR transport equation. After the point of stopping, a deceleration wave travels along the jet, upstream of which new decelerating self-similar profiles are identified for SDR and its directional components. Self-similarity also holds for dominant terms of the mean SDR transport equation.

The deceleration wave characteristic for SDR seems to travel at a speed similar to that corresponding to axial velocity, indicating that changes in turbulent mixing caused by jet stopping propagate concurrently with the velocity field. Behind the decelerating wave, the centreline SDR becomes proportional to the axial distance and inversely proportional to

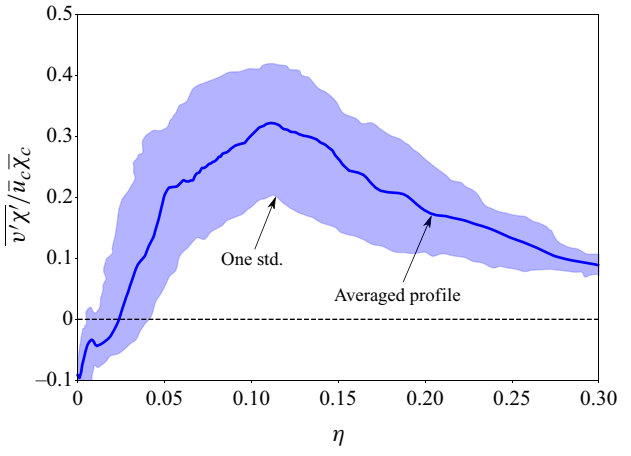

Figure 18. Normalised decelerating self-similar profile over $t/\tau = 50{-}69$ and $(x - x_0)/D = 14{-}28$ for $\overline{u'\chi'}$.

the square of time. The presence of the decelerating self-similar profiles is analysed first at two selected axial locations, then averaged over a wider range of axial locations. At inspected axial locations, radial profiles transition from the steady-state profiles to new decelerating self-similar ones. When profiles reach the decelerating self-similar state, they remain in place.

Decelerating SDR self-similar profiles show increased dissipation during jet deceleration, when compared to their steady-state counterparts. This suggests that enhanced entrainment evidenced after stopping leads, on average, to an increase in dissipation. For the mean SDR transport equation, budget terms associated with turbulent stretching of the scalar field and curvature effects on the scalar field remain dominant even when the jet is stopped. The temporal term, although not negligible, has a small contribution to the equation balance. Increase in dissipation after stopping is also reflected in the magnitude of terms V and VI, which are larger in magnitude when compared to their steady-state counterparts.

The assumption of decelerating self-similarity is re-validated by comparing the predicted turbulent transport term ($\overline{v'\chi'}$) with its DNS equivalent. The predicted slope and the $\overline{v'\chi'}$ radial profile are close to DNS data.

Three algebraic models for the mean SDR and the two dominant terms of the mean SDR transport equation are compared with actual DNS data. For the steady-state jet, scaling of the models satisfies self-similarity, and the resulting model coefficients agree with previous investigations. For the stopping jet, however, modification of the coefficients is necessary. Two types of modifications are proposed, both introducing a Re_t dependency. These two types satisfy the scaling given by self-similarity.

Acknowledgements. This research was carried out within the 'Nucleu' Programme, part of the National Plan for Research, Development and Innovation 2022–2027, carried out with the support of the Romanian Ministry of Research, Innovation and Digitalisation, grant no. 31N/2023, project no. PN23.12.02.01. Additional support was given by the Korea Institute of Energy Technology Evaluation and Planning (KETEP) and the Ministry of Trade, Industry & Energy (MOTIE) of the Republic of Korea (grant no. 20214000000310, Energy Innovation Research Center for Carbon-Neutral High-Efficiency Gas Turbine Combustion Technology). The authors are grateful for the computational support from the Korea Institute of Science and Technology Information (KISTI) for the Nurion cluster (KSC-2023-CRE-0241). Financial support from the EPSRC, UK grants EP/N509644/1, EP/R029369/1 and UKCTRF grant EP/L002698/1, is also gratefully acknowledged.

Declaration of interests. The authors report no conflict of interest.

Appendix A. Decelerating self-similar profile of $\overline{u'\chi'}$

Figure 18 shows the normalised decelerating self-similar profile that is averaged over $t/\tau = 50-69$ and $(x - x_0)/D = 14-28$ for $\overline{u'\chi'}$.

References

Aparece-Scutariu, V. & Shin, D. 2022 Spatial characteristics and modelling of mixture fraction variance and scalar dissipation rate in steady turbulent round jets. *Intl J. Heat Fluid Flow* **98**, 109048.

Ashurst, W.T., Kerstein, A.R., Kerr, R.M. & Gibson, C.H. 1987 Alignment of vorticity and scalar gradient with strain rate in simulated Navier–Stokes turbulence. *Phys. Fluids* **30** (8), 2343–2353.

Batchelor, G.K. 1953 *The Theory of Homogeneous Turbulence*. Cambridge University Press.

Bechlars, P. & Sandberg, R.D. 2017 Variation of enstrophy production and strain rotation relation in a turbulent boundary layer. *J. Fluid Mech.* **812**, 321–348.

Bogey, C., Cacqueray, N.D. & Bailly, C. 2009 A shock-capturing methodology based on adaptative spatial filtering for high-order non-linear computations. *J. Comput. Phys.* **228** (5), 1447–1465.

Borée, J., Atassi, N. & Charnay, G. 1996 Phase averaged velocity field in an axisymmetric jet subject to a sudden velocity decrease. *Exp. Fluids* **21** (6), 447–456.

Borghi, R. 1990 Turbulent premixed combustion: further discussions on the scales of fluctuations. *Combust. Flame* **80** (3–4), 304–312.

Bray, K.N.C., Peters, N., Libby, P.A. & Williams, F.A. 1994 *Turbulent Reacting Flows*. Academic Press.

Bremhorst, K. & Hollis, P.G. 1990 Velocity field of an axisymmetric pulsed, subsonic air jet. *AIAA J.* **28** (12), 2043–2049.

Buch, K.A. & Dahm, W.J.A. 1998 Experimental study of the fine-scale structure of conserved scalar mixing in turbulent shear flows. Part 2. $Sc \approx 1$. *J. Fluid Mech.* **364**, 1–29

Chakraborty, N., Champion, M., Mura, A. & Swaminathan, N. 2011 Scalar-dissipation-rate approach. In *Modelling Methods* (ed. K.N.C. Bray), pp. 110–127. Cambridge University Press.

Danaila, L., Antonia, R.A. & Burattini, P. 2012 Comparison between kinetic energy and passive scalar energy transfer in locally homogeneous isotropic turbulence. *Physica D* **241** (3), 224–231.

Deuse, M. & Sandberg, R.D. 2020 Different noise generation mechanisms of a controlled diffusion aerofoil and their dependence on Mach number. *J. Sound Vib.* **476**, 115317.

Dunstan, T.D., Minamoto, Y., Chakraborty, N. & Swaminathan, N. 2013 Scalar dissipation rate modelling for large eddy simulation of turbulent premixed flames. *Proc. Combust. Inst.* **34** (1), 1193–1201.

Feikema, D.A., Everest, D. & Driscoll, J.F. 1996 Images of dissipation layers to quantify mixing within a turbulent jet. *AIAA J.* **34** (12), 2531–2538.

Fuest, F., Barlow, R.S., Magnotti, G. & Sutton, J.A. 2018 Scalar dissipation rates in a turbulent partially-premixed dimethyl ether/air jet flame. *Combust. Flame* **188**, 41–65.

Geyer, D., Kempf, A., Dreizler, A. & Janicka, J. 2005 Scalar dissipation rates in isothermal and reactive turbulent opposed-jets: 1-D-Raman/Rayleigh experiments supported by LES. *Proc. Combust. Inst.* **30** (1), 681–689.

Gill, K., Marriner, C., Sison, K. & Zhao, H. 2005 In-cylinder studies of multiple diesel fuel injection in a single cylinder optical engine. *Tech. Rep.* 2005-01-0915. SAE Technical Paper.

Guest, P.G. 2012 *Numerical Methods of Curve Fitting*. Cambridge University Press.

Hawkes, E.R., Sankaran, R., Chen, J.H., Kaiser, S.A. & Frank, J.H. 2009 An analysis of lower-dimensional approximations to the scalar dissipation rate using direct numerical simulations of plane jet flames. *Proc. Combust. Inst.* **32** (1), 1455–1463.

Hill, W.G. & Greene, P.R. 1977 Increased turbulent jet mixing rates obtained by self-excited acoustic oscillations. *J. Fluids Eng.* **99** (3), 520–525.

Hussein, H.J., Capp, S.P. & George, W.K. 1994 Velocity measurements in a high-Reynolds-number, momentum-conserving, axisymmetric, turbulent jet. *J. Fluid Mech.* **258**, 31–75.

LaRue, J.C., John, C. & Libby, P.A. 1981 Thermal mixing layer downstream of half-heated turbulence grid. *Phys. Fluids* **24** (4), 597–603.

Janicka, J. & Peters, N. 1982 Prediction of turbulent jet diffusion flame lift-off using a pdf transport equation. In *Symposium (International) on Combustion*, Vol. 19, pp. 367–374. Elsevier.

Jones, W.P. 1994 Turbulence modelling and numerical solution methods for variable density and combusting flows. In *Turbulent Reacting Flows* (P.A. Libby & F.A. Williams), pp. 309–374. Academic Press, London.

Jones, W.P. & Musonge, P. 1988 Closure of the Reynolds stress and scalar flux equations. *Phys. Fluids* **31** (12), 3589–3604.

JUNEJA, A. & POPE, S.B. 1996 A DNS study of turbulent mixing of two passive scalars. *Phys. Fluids* **8** (8), 2161–2184.
KAISER, S.A. & FRANK, J.H. 2007 Imaging of dissipative structures in the near field of a turbulent non-premixed jet flame. *Proc. Combust. Inst.* **31** (1), 1515–1523.
KARPETIS, A.N. & BARLOW, R.S. 2002 Measurements of scalar dissipation in a turbulent piloted methane/air jet flame. *Proc. Combust. Inst.* **29** (2), 1929–1936.
KENNEDY, C.A., CARPENTER, M.H. & LEWIS, R.M. 2000 Low-storage, explicit Runge–Kutta schemes for the compressible Navier–Stokes equations. *Appl. Numer. Maths* **35** (3), 177–219.
KENNEDY, C.A. & GRUBER, A. 2008 Reduced aliasing formulations of the convective terms within the Navier–Stokes equations for a compressible fluid. *J. Comput. Phys.* **227** (3), 1676–1700.
KIM, J.W. & LEE, D.J. 2000 Generalized characteristic boundary conditions for computational aeroacoustics. *AIAA J.* **38** (11), 2040–2049.
KLEIN, M., SADIKI, A. & JANICKA, J. 2003 A digital filter based generation of inflow data for spatially developing direct numerical or large eddy simulations. *J. Comput. Phys.* **186** (2), 652–665.
KOLLA, H., ROGERSON, J.W., CHAKRABORTY, N. & SWAMINATHAN, N. 2009 Scalar dissipation rate modeling and its validation. *Combust. Sci. Technol.* **181** (3), 518–535.
KOLMOGOROV, A.N. 1962 A refinement of previous hypotheses concerning the local structure of turbulence in a viscous incompressible fluid at high Reynolds number. *J. Fluid Mech.* **13** (1), 82–85.
LANGELLA, I. & SWAMINATHAN, N. 2016 Unstrained and strained flamelets for LES of premixed combustion. *Combust. Theor. Model.* **20** (3), 410–440.
LANGELLA, I., SWAMINATHAN, N., GAO, Y. & CHAKRABORTY, N. 2015 Assessment of dynamic closure for premixed combustion large eddy simulation. *Combust. Theor. Model.* **19** (5), 628–656.
LIBBY, P.A. & BRAY, K.N.C. 1980 Implications of the laminar flamelet model in premixed turbulent combustion. *Combust. Flame* **39** (1), 33–41.
LUMLEY, J.L. 1976 Modelling buoyancy-driven mixed layers. *J. Atmos. Sci.* **33** (10), 1974–1988.
LUMLEY, J.L. & KHAJEH-NOURI, B. 1975 Computational modeling of turbulent transport. In *Turbulent Diffusion in Environmental Pollution* (ed. F.N. Frenkiel & R.E. Munn), vol. 18, pp. 169–192. Elsevier.
MA, B.-K. & WARHAFT, Z. 1986 Some aspects of the thermal mixing layer in grid turbulence. *Phys. Fluids* **29** (10), 3114–3120.
MANTEL, T. & BORGHI, R. 1994 A new model of premixed wrinkled flame propagation based on a scalar dissipation equation. *Combust. Flame* **96** (4), 443–457.
MASTORAKOS, E., BARITAUD, T.A. & POINSOT, T.J. 1997 Numerical simulations of autoignition in turbulent mixing flows. *Combust. Flame* **109** (1–2), 198–223.
MCMANUS, T.A. & SUTTON, J.A. 2023 Conditional analysis of temperature and strain rate effects on dissipation structure in turbulent non-premixed jet flames. *Proc. Combust. Inst.* **39** (2), 2419–2427.
MI, J., NOBES, D.S. & NATHAN, G.J. 2001 Influence of jet exit conditions on the passive scalar field of an axisymmetric free jet. *J. Fluid Mech.* **432**, 91–125.
MULLA, I.A. & HARDALUPAS, Y. 2022 Measurement of instantaneous fully 3D scalar dissipation rate in a turbulent swirling flow. *Exp. Fluids* **63** (11), 173.
MURA, A. & BORGHI, R. 2003 Towards an extended scalar dissipation equation for turbulent premixed combustion. *Combust. Flame* **133** (1–2), 193–196.
MUSCULUS, M.P.B. 2009 Entrainment waves in decelerating transient turbulent jets. *J. Fluid Mech.* **638**, 117–140.
O'CONNOR, J. & MUSCULUS, M. 2013 Post injections for soot reduction in diesel engines: a review of current understanding. *SAE Intl J. Engines* **6** (1), 400–421.
OVERHOLT, M.R. & POPE, S.B. 1996 Direct numerical simulation of a passive scalar with imposed mean gradient in isotropic turbulence. *Phys. Fluids* **8** (11), 3128–3148.
POINSOT, T. & VEYNANTE, D. 2005 *Theoretical and Numerical Combustion*. R.T. Edwards, Inc.
POPE, S.B. 2000 *Turbulent Flows*. Cambridge University Press.
SAINI, D. & SANDBERG, R.D. 2020 Simulations of compressibility effects in centrifugal buoyancy-induced flow in a closed rotating cavity. *Intl J. Heat Fluid Flow* **85**, 108656.
SANDBERG, R.D. 2011 An axis treatment for flow equations in cylindrical coordinates based on parity conditions. *Comput. Fluids* **49** (1), 166–172.
SANDBERG, R.D. 2013 Direct numerical simulations for flow and noise studies. *Procedia Engng* **61**, 356–362.
SANDBERG, R.D. & SANDHAM, N.D. 2006 Nonreflecting zonal characteristic boundary condition for direct numerical simulation of aerodynamic sound. *AIAA J.* **44** (2), 402–405.
SANDBERG, R.D., SANDHAM, N.D. & SUPONITSKY, V. 2012 DNS of compressible pipe flow exiting into a coflow. *Intl J. Heat Fluid Flow* **35**, 33–44.

SCHUMACHER, J., SREENIVASAN, K.R. & YEUNG, P.K. 2005 Very fine structures in scalar mixing. *J. Fluid Mech.* **531**, 113–122.

SHIN, D., ASPDEN, A.J., APARECE-SCUTARIU, V. & RICHARDSON, E.S. 2023 Unsteady self-similarity of jet fluid age and mass fraction. *Phys. Fluids* **35** (1), 015139.

SHIN, D., ASPDEN, A.J. & RICHARDSON, E.S. 2017 Self-similar properties of decelerating turbulent jets. *J. Fluid Mech.* **833**, R1.

SHIN, D.-H., SANDBERG, R.D. & RICHARDSON, E.S. 2017*b* Self-similarity of fluid residence time statistics in a turbulent round jet. *J. Fluid Mech.* **823**, 1–25.

SOULOPOULOS, N., HARDALUPAS, Y. & TAYLOR, A.M.K.P. 2014 Scalar dissipation rate measurements in a starting jet. *Exp. Fluids* **55** (3), 1685.

SOULOPOULOS, N., HARDALUPAS, Y. & TAYLOR, A.M.K.P. 2015 Mixing and scalar dissipation rate statistics in a starting gas jet. *Phys. Fluids* **27** (12), 125103.

SREENIVASAN, K.R. 1991 On local isotropy of passive scalars in turbulent shear flows. *Proc. R. Soc. Lond. A: Math. Phys. Sci.* **434** (1890), 165–182.

SU, L.K. & CLEMENS, N.T. 1999 Planar measurements of the full three-dimensional scalar dissipation rate in gas-phase turbulent flows. *Exp. Fluids* **27** (6), 507–521.

SWAMINATHAN, N. & BRAY, K.N.C. 2005 Effect of dilatation on scalar dissipation in turbulent premixed flames. *Combust. Flame* **143** (4), 549–565.

TENNEKES, H. & LUMLEY, J.L. 1972 *A First Course in Turbulence*. MIT Press.

WARHAFT, Z. 2000 Passive scalars in turbulent flows. *Annu. Rev. Fluid Mech.* **32** (1), 203–240.

ZHAO, Y. & SANDBERG, R.D. 2021 High-fidelity simulations of a high-pressure turbine stage: effects of Reynolds number and inlet turbulence. In *Turbo Expo: Power for Land, Sea, and Air*, V02BT32A004. American Society of Mechanical Engineers.